Delft University of Technology

Lactate controls cancer stemness and plasticity through epigenetic regulation

Nguyen, Nguyen T.B.; Gevers, Sira; Kok, Rutger N.U.; Neikes, Hannah; Betjes, Max A.; Drost, Jarno; Tans, Sander J.; Burgering, Boudewijn M.T.; Rodríguez Colman, Maria J.; More Authors

Important note
To cite this publication, please use the final published version (if applicable).
Please check the document version above.

Lactate controls cancer stemness and plasticity through epigenetic regulation

Graphical abstract
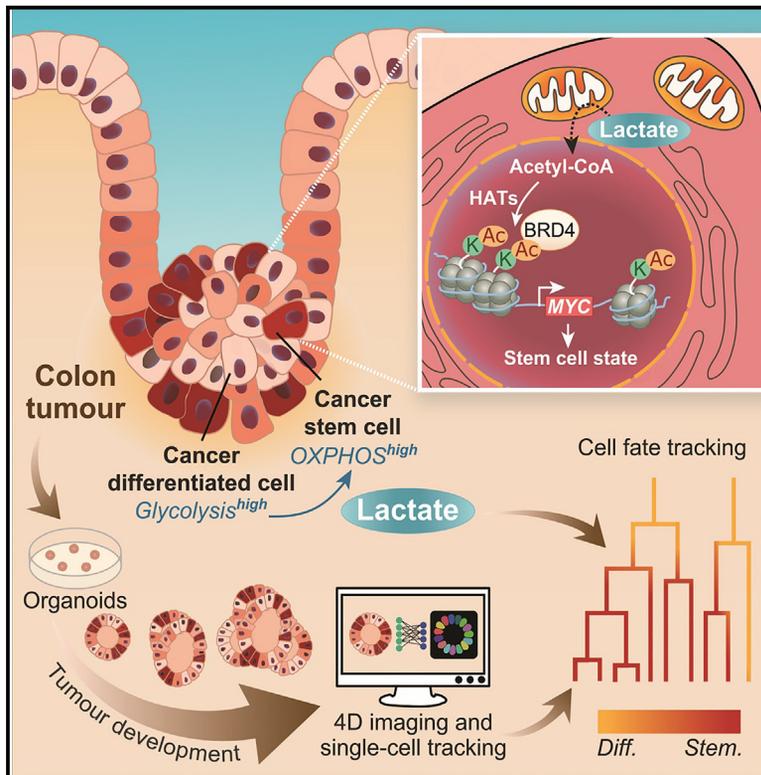
Authors

Nguyen T.B. Nguyen, Sira Gevers,
Rutger N.U. Kok, ..., Sander J. Tans,
Boudewijn M.T. Burgering,
Maria J. Rodríguez Colman

Correspondence

m.j.rodriguezcolman@umcutrecht.nl

In brief

Using fluorescent reporters and machine learning, Nguyen et al. traced cell types, metabolism, and lineages in tumor organoids, revealing that lactate regulates tumor development by inhibiting cancer cell differentiation and promoting dedifferentiation into a stem cell state. Mechanistically, lactate-induced metabolic reprogramming enhances histone acetylation, epigenetically activating MYC, shaping tumor dynamics.

Highlights

- Single-cell tracking of tumor organoids maps cell-type transitions and metabolism

- Cancer stem and differentiated cells vary in glycolytic rates and exchange lactate

- Lactate drives cancer stem cell identity by disrupting cell fate commitment

- Lactate metabolism epigenetically activates the *MYC* oncogene

CellPress

Article

Lactate controls cancer stemness and plasticity through epigenetic regulation

Nguyen T.B. Nguyen,[1,3] Sira Gevers,[1,3] Rutger N.U. Kok,[1,3] Lotte M. Burgering,[1,3] Hannah Neikes,[2,3] Ninouk Akkerman,[4,8] Max A. Betjes,[5] Marlies C. Ludikhuize,[1] Can Gulersonmez,[1] Edwin C.A. Stigter,[1] Yvonne Vercoulen,[1] Jarno Drost,[3,6] Hans Clevers,[3,4,8] Michiel Vermeulen,[2,3] Jeroen S. van Zon,[5] Sander J. Tans,[5,7] Boudewijn M.T. Burgering,[1,3] and Maria J. Rodríguez Colman[1,3,9,*]

[1]Molecular Cancer Research, Center for Molecular Medicine, University Medical Center Utrecht, Heidelberglaan 100, 3584 CG Utrecht, the Netherlands
[2]Department of Molecular Biology, Faculty of Science, Radboud Institute for Molecular Life Sciences, Oncode Institute, Radboud University Nijmegen, Nijmegen 6525 GA, the Netherlands
[3]Oncode Institute, Utrecht, the Netherlands
[4]Hubrecht Institute, Royal Netherlands Academy of Arts and Sciences, University Medical Center Utrecht, Utrecht, the Netherlands
[5]AMOLF, Amsterdam, the Netherlands
[6]Princess Máxima Center for Pediatric Oncology, Heidelberglaan 25, 3584 CS Utrecht, the Netherlands
[7]Bionanoscience Department, Kavli Institute of Nanoscience Delft, Delft University of Technology, Delft, the Netherlands
[8]Present address: Roche Pharmaceutical Research and Early Development, Basel, Switzerland
[9]Lead contact
*Correspondence: m.j.rodriguezcolman@umcutrecht.nl
https://doi.org/10.1016/j.cmet.2025.01.002

SUMMARY

Tumors arise from uncontrolled cell proliferation driven by mutations in genes that regulate stem cell renewal and differentiation. Intestinal tumors, however, retain some hierarchical organization, maintaining both cancer stem cells (CSCs) and cancer differentiated cells (CDCs). This heterogeneity, coupled with cellular plasticity enabling CDCs to revert to CSCs, contributes to therapy resistance and relapse. Using genetically encoded fluorescent reporters in human tumor organoids, combined with our machine-learning-based cell tracker, CellPhenTracker, we simultaneously traced cell-type specification, metabolic changes, and reconstructed cell lineage trajectories during tumor organoid development. Our findings reveal distinctive metabolic phenotypes in CSCs and CDCs. We find that lactate regulates tumor dynamics, suppressing CSC differentiation and inducing dedifferentiation into a proliferative CSC state. Mechanistically, lactate increases histone acetylation, epigenetically activating MYC. Given that lactate's regulation of MYC depends on the bromodomain-containing protein 4 (BRD4), targeting cancer metabolism and BRD4 inhibitors emerge as a promising strategy to prevent tumor relapse.

INTRODUCTION

Epithelial tissue maintenance relies on self-renewing stem cells, with mutations in stemness-regulating pathways causing uncontrolled cell proliferation and tumor formation.[1] In the intestine, WNT activity is the main regulator of the stem cell state, and its overactivation drives tumorigenesis.[2–4] Despite a general WNT overactivation and the occurrence of additional mutations, lineage tracing experiments showed that colorectal tumors retain some of the hierarchical organization of their tissue of origin, with the presence of cancer stem cells (CSCs) and cancer differentiated cells (CDCs).[5] CSCs, characterized by higher WNT activity and proliferation, differentiate giving rise to CDCs.[5–7] While the role of CSCs in fueling tumor growth is well established, CDCs' role in tumorigenesis remains largely unexplored, despite their widespread presence across tumors implying a functional contribution to colorectal cancer (CRC) progression.[6,8] In agree-

ment, this cellular diversity is required for successful tumor growth and metastatic outgrowth.[9,10] Moreover, cell plasticity, entailing the dedifferentiation of CDCs to CSCs, has been observed upon the genetic depletion of CSCs, thereby restoring tumor growth potential.[6,8,11] Interestingly, hierarchical cellular lineages (CSCs and CDCs) and cell plasticity are observed both in vivo and in vitro organoids,[6,8,11] indicating that tumor cells inherently orchestrate these processes. Despite their significant impact on therapy resistance and cancer relapse,[12,13] neither the advantages of these processes nor their regulatory mechanisms are completely understood.

Previous studies by others and us showed that different intestinal cell types display distinct metabolic phenotypes.[14–16] Metabolic changes play a role in stem cell differentiation, and interestingly, lactate is exchanged between intestinal cell types.[14–16] However, whether cell-type-specific metabolic phenotypes occur in tumors and how they impact on cell fate decisions,

such as stemness, differentiation, and plasticity, remains unknown.

In this study, we investigated how lactate, a metabolite abundantly produced by tumors, regulates tumor development. We developed a machine learning imaging-based method, CellPhenTracker, which enables to simultaneously track and trace cell-type specification and metabolism during tumor organoid development, with single-cell and high temporal resolution. This method revealed differential lactate metabolism between CSCs and CDCs, suggesting lactate exchange between these cells. Furthermore, we observed that lactate levels, resembling the tumor microenvironment, increase the population of CSCs by inhibiting differentiation and by activating CDCs to regress to a proliferative CSC state. This process is mediated by the epigenetic regulation of MYC and dependent on the epigenetic reader BRD4. Altogether, our findings indicate that lactate resulting from the Warburg effect is a key intrinsic regulator of tumor development by maintaining the CSC population through the epigenetic regulation of the *MYC* oncogene.

RESULTS

CSCs and CDCs display differential lactate metabolism

Previous work from others and us showed that in the mouse intestine stem cells and differentiated cells exhibit distinct metabolic phenotypes, that cell types can interact via lactate, and that metabolic changes can drive stem cell differentiation.[15,17,18] We interrogated whether such metabolic differences occur in the human colon and in colon tumors. Immunostainings of colon tissue showed that keratin 20 (KRT20)-positive differentiated cells at the top of the crypt display higher levels of the monocarboxylate transporter 4 (MCT4), compared with KRT20-negative KI67-positive proliferative stem cells, which reside at the bottom of the crypt (Figures 1A and S1A). MCT4 has a lower affinity for lactate than MCT1, and it is more highly expressed in glycolytic tissues than in normal tissues.[19,20] Thus, increased levels of MCT4 may indicate differentiated cells being more glycolytic compared with stem cells. Similarly, in tumor cells, MCT4 levels were higher in KRT20-positive CDCs, whereas MCT1 varied across cell populations (Figures 1A and S1C–S1E). Therefore, despite the Warburg effect being considered a widely conserved phenotype of cancer cells,[21] the observed differences in MCT4 levels suggested the occurrence of metabolic differences between cells within tumors.

To further investigate cell-type metabolic differences in tumors, we analyzed single-cell RNA sequencing data from sixty tumors collected in three different studies.[22–24] Cell-type signature analysis on epithelial tumor cells revealed the presence of tumor cell types resembling the primary intestinal cell types: stem-cell-like, transit-amplifying (TA)-cell-like, enterocyte-like, and secretory-like cells (Figures 1B and S1B). Consistent with our prior observations, both *KRT20* and *MCT4* were highly expressed in differentiated enterocyte-like cells, while the stem cell marker *ASCL2* and the proliferation marker *KI67* were highly expressed in TA-like cells, resembling a CSC phenotype (Figure S1F). We analyzed the scores for various metabolic signatures across the tumor cell types and observed that the glycolytic score was elevated in differentiated enterocytes, whereas TA-like tumor cells exhibited the highest scores for mitochondrial metabolism (oxidative phosphorylation [OXPHOS]) (Figures 1C and S1G). These differ-

ences in gene expression suggested that tumor cells may engage different metabolic programs. Next, we explored the functional implications of these differences. Organoids, derived from healthy or tumor tissue, recapitulate tissue architecture and cellular dynamics and allow manipulation to prove causality.[25,26] We established human organoid models to monitor cell-type and metabolic diversification during tumor development. Tumor progression organoids (TPOs) were previously engineered to carry the most frequent mutations in CRC. TPO3 carries *adenomatous polyposis coli* (*APC*)[KO], *KRAS*[G12D], and *P53*[KO], while TPO4 additionally carries *SMAD4*[KO].[27] We introduced a WNT-signaling-based stem cell reporter (STAR[28]) and the metabolic sensors SoNar,[29] FLII12Pglu-700uDelta6,[30,31] and Laconic,[32] which report for NAD+/NADH, glucose, and lactate, respectively. These sensors were validated for their use in organoids (Figures 1J, S1H, and S1Q, respectively). STAR-positive cells (STARpos) show higher expression of stem cell and proliferation markers, while STAR-negative cells (STARneg) showed higher expression of differentiation markers (Figure S1I). Therefore, STARpos cells resemble the tumors stem and TA-like cells, while STARneg cells represent differentiated cancer cells, henceforth referred to as CSCs and CDCs, respectively.

In cells, the NAD+/NADH ratio responds to the glycolytic flux since the conversion of pyruvate to lactate is in equilibrium with NAD+/NADH.[29,33–36] In line with this, the sequential addition of lactate and pyruvate to SoNar organoids showed a drop in the NAD+/NADH ratio in response to lactate, followed by its increase upon pyruvate (Figure S1H). Single-cell SoNar analysis revealed that CSCs have significantly higher NAD+/NADH ratios compared with CDCs cells, a difference consistently observed throughout tumor organoid development (Figures 1D, 1E, and S1J). These results suggest differences in glycolysis between CSCs and CDCs. Furthermore, MCT4 levels were higher in CDCs than in CSCs, while the abundance of mitochondria and the expression of *mitochondrial transcription factor A* (*TFAM*) were higher in CSCs (Figures S1I and S1L–S1O).

To explore this further, we employed the Laconic reporter. Single-cell analysis revealed higher levels of lactate in CDCs when compared with CSCs (Figures 1F and 1G). Notably, inhibition of MCT transporters decreased the secretion of lactate to the medium and lead to the build-up of lactate to higher levels in CDCs, indicating higher glycolytic rates in CDCs than in CSCs (Figures 1H and S1K). Interestingly, no significant differences were found in basal levels of glucose neither in glucose uptake between CDCs and CSCs (Figures S1P–S1R). The observation that CDCs were more prone to lactate production than CSCs, while displaying comparable glucose uptake, suggests that CSCs may divert glycolytic intermediates toward anabolic processes to meet the demands of cell proliferation at the expense of lactate production. The final step of glycolysis converting pyruvate to lactate occurs concomitantly with the oxidation of NADH to NAD+. Therefore, we questioned how CSCs can maintain a higher NAD+/NADH ratio (Figures 1D and 1E). Mitochondria contribute to the NAD+/NADH cellular balance by the activity of mitochondrial NAD+/NADH shuttles.[37] Inhibition of mitochondrial activity with oligomycin reduced the NAD+/NADH ratio in all cells, with a more pronounced effect in CSCs (Figures 1I, S1S, and S1T), indicating a stronger contribution of mitochondria to the NAD+/NADH ratio in CSCs.
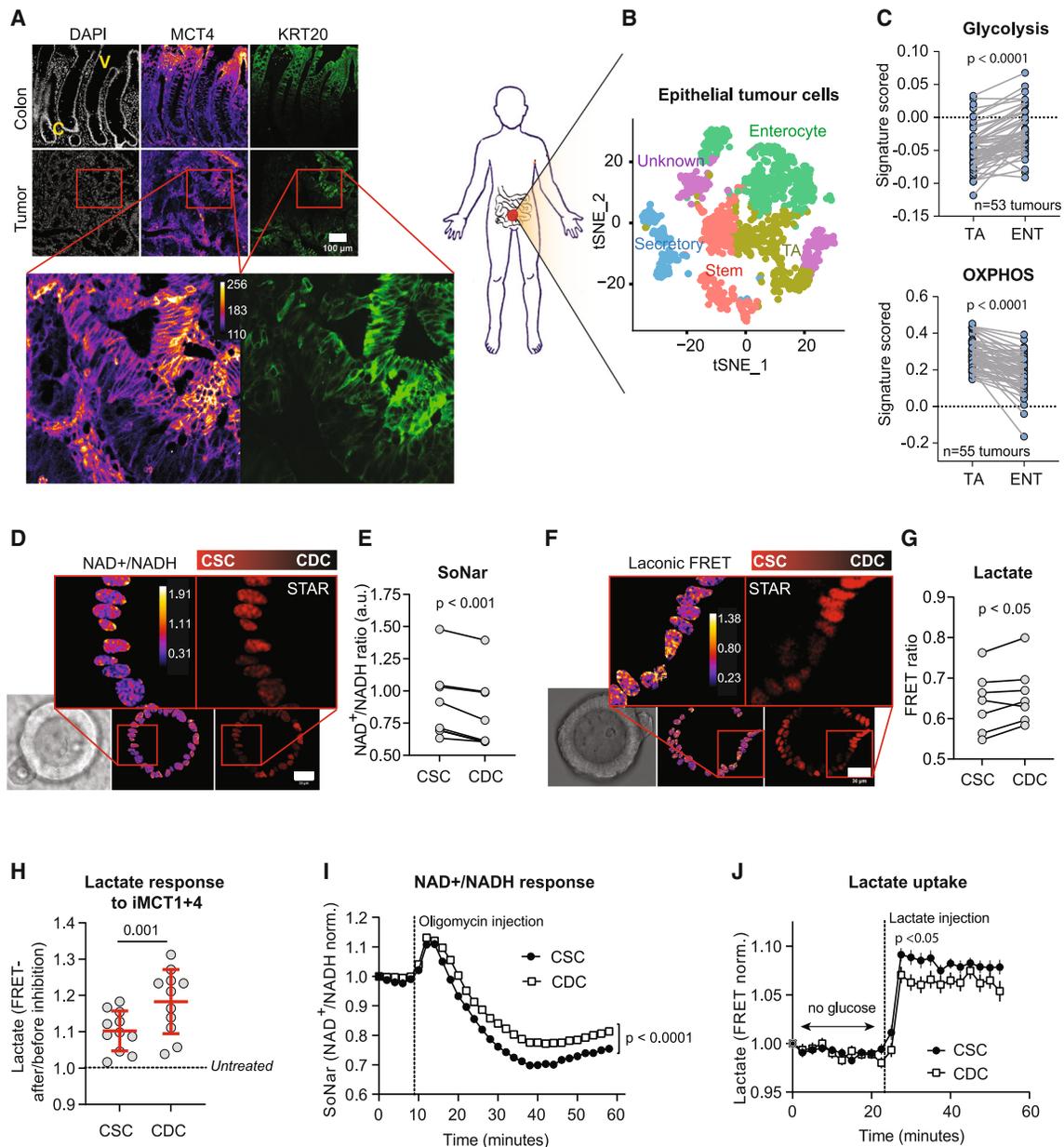
Figure 1. CSCs and CDCs display differential lactate metabolism

(A) Representative images out of three healthy and tumor colon biopsies stained with MCT4 and KRT20. Nuclei are labeled with DAPI (V, villi side; C, crypt zones; scale bar, 100 μm).

(B) Representative t-SNE plot showing epithelial cancer cell types classified and annotated using scType. Sixty single-cell RNA sequencing (scRNA-seq) CRC datasets were analyzed.

(C) Average glycolysis and OXPHOS scores calculated for TA cells (TA) and enterocytes (ENT) derived from different CRC scRNA-seq datasets (glycolysis $n = 53$; OXPHOS $n = 55$ tumors; paired t test). Signature details can be found in Table S6.

(D and E) Live imaging of nuclear NAD^+/NADH ratio (H2B-SoNar 488 ex/405 ex) and its quantification in CSCs and CDCs in TPO3 ($n = 8$, paired t test, scale bar, 30 μm).

(F and G) Live imaging of nuclear lactate levels with Laconic-NLS, a Förster resonance energy transfer (FRET) biosensor, and its quantification (mTFP/Venus) in CSCs and CDCs in TPO3 ($n = 7$ across 4 experiments, paired t test, scale bar, 30 μm).

(H) Laconic-NLS FRET response (post-treatment/pre-treatment FRET ratio) comparing CSCs and CDCs after 3 h of treatment with 10 μM syrosingopine (iMCT1 + 4) ($n = 11$ TPO3 organoids across 2 experiments, mean ± SD, paired t test).

(I) SoNar (nuclear NAD^+/NADH) response between CSCs and CDCs following OXPHOS inhibition by 2 μM oligomycin injection (each group $n = 62$ cells, mean ± SEM, unpaired t test with significant differences from time point 30). A representative out of 3 analyzed organoids is shown.

(J) Lactate uptake capacity (injected 10 mM of L-lactate) between CSCs ($n = 58$) and CDCs ($n = 55$) in TPO3 organoid, which were pre-cultured in glucose-free medium for 3 h (mean ± SEM, unpaired t tests at timepoint 26). A representative organoid of 6 analyzed organoids is shown.

See also Data S1 and Figure S1.
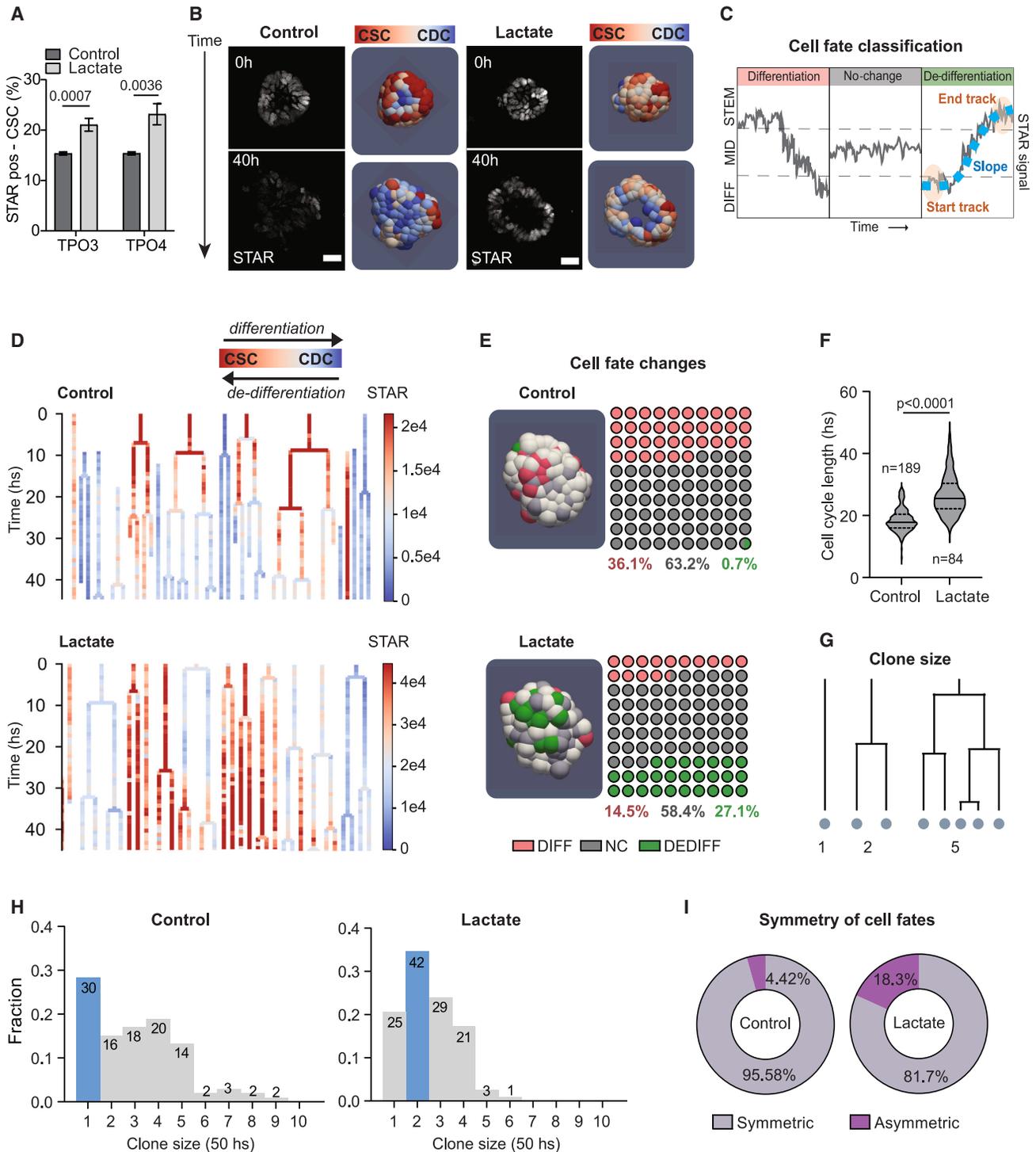
Figure 2. Lactate increases CSCs by repressing differentiation and inducing dedifferentiation

(A) Fluorescence-activated cell sorting (FACS) analysis of STAR-based CSC percentages in TPO3 and TPO4 after 5 days of culture under control or lactate conditions (mean ± SEM, TPO3 n = 13, TPO4 n = 12, paired t test).

(B) Time-lapse imaging of TPO3-STAR-NLS organoids grown in control or lactate (scale bar, 30 μm).

(C) Schematic representation of the cell fate classification strategy, based on start and end STAR values and on the slope of the change over time.

(D) Representative lineage trees show single-cell STAR values during organoid development in either control or lactate. Each line represents one cell and branching represents cell division. Track endings indicate either cell death (<2%) or cells moving out of the imaging field.

(legend continued on next page)

The conversion of pyruvate to lactate and vice-versa is catalyzed by the tetrameric complex of lactate dehydrogenases A and B (LDHA and LDHB). The LDH isoform expression can reflect the local metabolic state, with higher LDHB levels in aerobic conditions, with exceptions, such as in the liver.[38,39] Differences in *LDHB/LDHA* expression between CSCs and CDCs (Figure S1I), prompted us to investigate the uptake of lactate. Lactate uptake was observed in all cells. Notably, CSCs showed higher uptake capacity than CDCs (Figures 1J and S1U). Interestingly, lactate uptake was inhibited by the dual inhibition of MCT1 and MCT4; while inhibition of either transporter had no effect (Figures S1V and S1W). Moreover, MCT1 inhibition did not rescue the elevated lactate uptake observed in CSCs (Figure S1X). Instead, lactate uptake capacity inversely correlated with basal lactate levels (Figure S1Y). As shown, CSCs have lower lactate levels (Figures 1F and 1G), suggesting that their higher lactate uptake capacity is driven by a steeper metabolite gradient across the CSC cell membrane. Altogether, live imaging analyses revealed that while both cell types exhibit glycolytic and mitochondrial activity, glucose is metabolized differently between CSCs and CDCs. Furthermore, the elevated lactate production by CDCs and the higher lactate uptake capacity in CSCs suggest a metabolic interaction in which CDCs secrete lactate that is taken up by oxidative CSCs. These observations prompted us to investigate the role of lactate in tumor development.

Lactate increases CSCs by repressing differentiation and inducing dedifferentiation

As a consequence of the Warburg effect, the tumor microenvironment is characterized by low glucose and elevated lactate levels that can build up to 30 mM.[40–42] Our findings indicate that CDCs and CSCs interact through lactate. Therefore, we investigated the effect of lactate in tumor development. Strikingly, we found that lactate (23 mM lactate supplemented with 0.5 mM of glucose) significantly increases the CSC population (Figure 2A). Consistent with this, lactate decreased the expression of differentiation markers and increased expression of stem cell markers, with a more pronounced effect in TPO3 than in TPO4 (Figure S2A), which may relate to the higher baseline stemness observed in TPO4 in control conditions (Figures S2J and S2K). Lactate induction of CSCs is not due to the lower concentration of glucose in this condition, as decreasing glucose availability on its own failed to recapitulate the phenotype (Figure S2B). Furthermore, inhibition of MCT transporters led to intracellular lactate accumulation and, remarkably, increased the number of CSCs (Figures 1H, S2C, and S2D), indicating that not only extracellular lactate but also intrinsic lactate production promotes CSC identity.

An increase in the stem cell population is typically associated with reduced stem cell differentiation. However, cell plasticity introduces additional dynamics: intestinal damage, inflammation, or stem cell ablation can trigger the regression of differentiated cells to the stem cell state, a process referred to as dedifferentiation.[6,43] To investigate the mechanisms by which lactate induces stem cells, we performed 4D imaging of tumor organoid development. We created CellPhenTracker upon the foundation of OrganoidTracker.[44] This machine learning-based tool allows single-cell tracking and fluorescent intensity quantification, enabling lineage reconstruction and the assessment of cell identity and metabolic state from time-lapse imaging (click here Video S1). By analyzing the STAR signal over time, we classified all cells as either differentiating, dedifferentiating, or unchanged (Figure 2C). We found that in control conditions, the fraction of CSCs in the organoids decreased over time, which was further supported by gene expression analysis (Figures 2B, 2D, S2E, and S2F). This decrease was caused by cell differentiation, with 36% of all cells transitioning to a differentiated state (Figures 2D and 2E). Dedifferentiation was rare, observed in less than 1% of all events (Figure 2E). Notably, under lactate conditions, cell differentiation was significantly reduced by 50%, accompanied by a striking increase in dedifferentiation, with 27% of all events exhibiting this phenomenon (Figures 2B, 2D, 2E, and S2E). These results indicate that lactate-induced CSCs result from both the inhibition of differentiation and, remarkably, the induction of CDCs to regress to the CSC state.

In control conditions, 5% of all cells undergo mitosis within 1 h supporting growth (Figure S2G). When grown on lactate, no significant differences were found in the total percentage of mitotic cells (Figure S2G). However, the cell-cycle length significantly increased when grown in lactate (Figure 2F), possibly due to the demands of glucose for anabolic processes supporting cell division. One might anticipate that a longer cell cycle would lead to slower organoid growth; however, organoid size was not significantly different across conditions (Figures S3O, S3P, and S3V). To explain this observation, we examined clone sizes—the number of offspring that a single cell produces after a defined amount of time (50 h) (Figure 2G). Interestingly, we noted a decrease in the fraction of non-dividing cells (clone size 1) and the concomitant increase in the fraction of proliferating cells when grown on lactate (clone size ≥ 2) (Figure 2H). Due to the longer cell cycle induced by lactate the number of large clones (clone size > 4) was reduced. Thus, although lactate induces longer cell cycles, its effect on increasing the number of proliferative CSCs balances out the occurrence of differential growth rates when compared with control.

In homeostatic conditions, intestinal stem cells divide symmetrically, resulting in two daughter cells with the same fate: both will differentiate or remain stem cells.[45–49] These dynamics, crucial for

---

(E) Quantification of cell fate changes in control (*n* = 7) and lactate (*n* = 4) TPO3 organoids (see Table S2). Digital reconstruction of representative organoids depicting cell fate change. Pink, green, and gray represent differentiation (DIFF), dedifferentiation (DEDIFF), or no change (NC) in cell fate, respectively. White cells are undefined (mean, Mann-Whitney test, *p* value of control vs. lactate DIFF: 0.073, DEDIFF: 0.003, and NC: 0.65).

(F) Cell-cycle length of cells (hours) from time-lapse imaging of TPO3 in control or lactate medium (median and quartiles, Mann-Whitney test).

(G) Schematic representation of clone sizes.

(H) Clone size distributions of all lineages of TPO3 organoids cultured in control (*n* = 3) or lactate (*n* = 3). Each lineage tree was recorded for a minimum of 50 h.

(I) Quantification of cell fate symmetry between sister-pairs in control or lactate TPO3 organoids. Percentages represent averages derived from all organoids within each respective group (control *n* = 8, lactate *n* = 4, two-way ANOVA: asymmetric and symmetric *p* < 0.001).

In all panels, control refers to 12 mM glucose, while lactate refers to 23 mM lactate + 0.5 mM glucose.
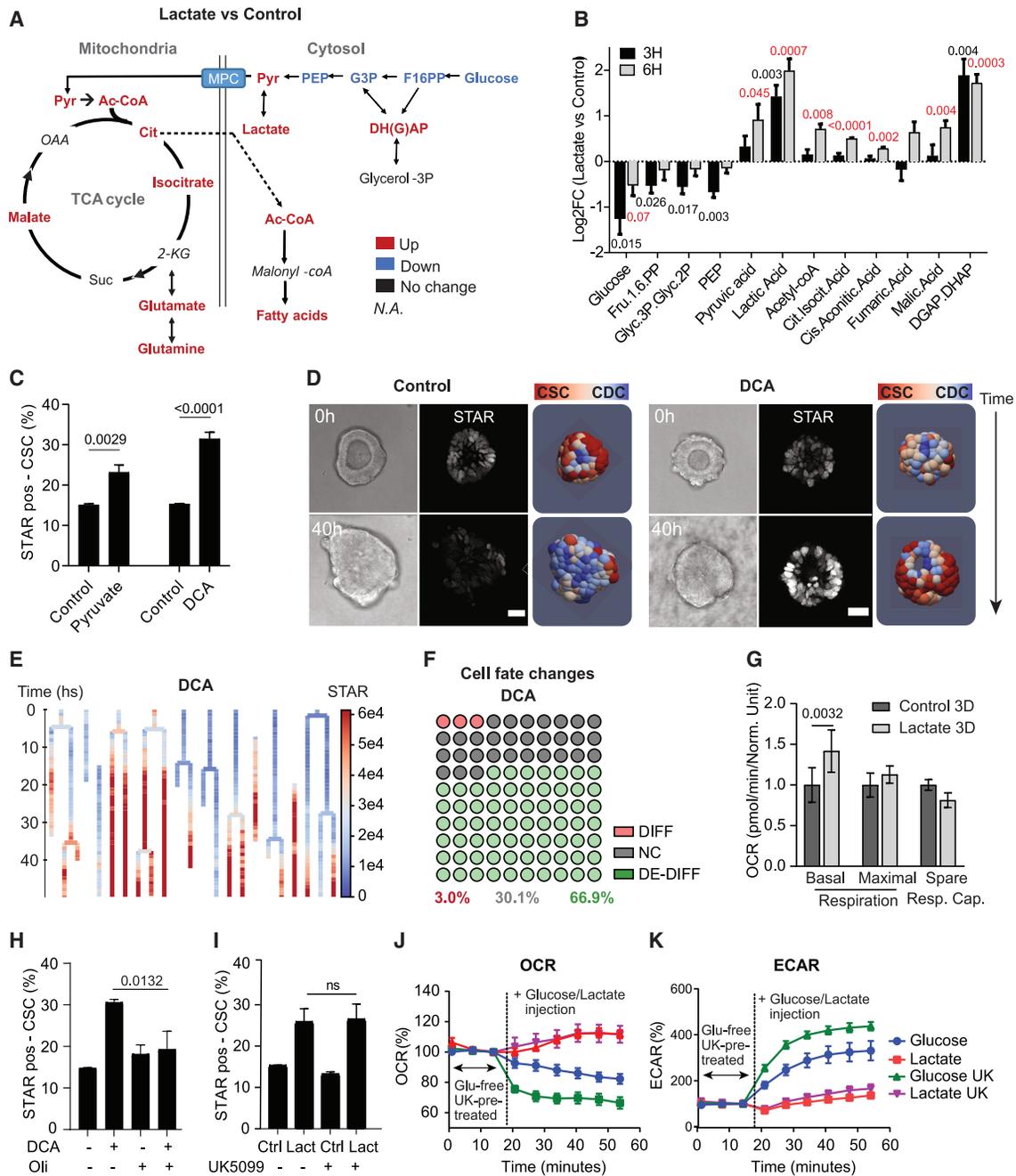
See also Data S1, Video S1, and Figure S2.

Figure 3. Lactate rewires metabolism and induces stemness independently of mitochondria pyruvate import

(A) Schematic representation of metabolomics of TPO3 grown in lactate vs. control. Red, blue, and black indicate upregulated, downregulated, and unchanged metabolites, respectively.

(B) Metabolomics analysis of TPO3 organoids cultured on lactate for 3 and 6 h compared with control organoids ($n = 4$–6 replicates of 2 independent experiments, one-sample t test).

(C) FACS analysis of STAR-based CSC percentages in TPO3 after 3-day culture on pyruvate or 20 mM DCA (pyruvate $n = 8$, DCA $n = 17$, paired t test).

(D) Time-lapse imaging of TPO3 development of control and DCA (20 mM) treated organoids (scale bar, 30 μm).

(E) Representative lineage trees show single-cell STAR dynamics during organoid development in DCA-treated TPO3 (20 mM). Each line represents one cell and branching represents cell division. Track endings indicate either cell death (<2%) or cells moving out of the imaging field.

(F) Quantification of cell fate changes: differentiation (DIFF), dedifferentiation (DEDIFF), and no change (NC) during DCA-treated TPO3 development (20 mM, $n = 3$ organoids, see Table S2). Control values are shown in Figure 2E (mean, Mann-Whitney test, p value control vs. DCA DIFF: 0.017, DEDIFF: 0.008, and NC: 0.017).

(G) Seahorse analysis of mitochondrial respiration in TPO3 grown in control or lactate for 3 days ($n = 5$, paired t test).

(H) FACS analysis of CSC percentages based on STAR signal of control and DCA-treated TPO3 (20 mM DCA for 3 days) and treated or not with oligomycin (Oli, 1 μM, 40 h) ($n = 5$, one-way ANOVA).

(legend continued on next page)

maintaining homeostasis and preventing the exhaustion of the stem cell pool, have been extensively studied in mice and in organoids, that faithfully recapitulate the process.[45,48] However, how these dynamics change in tumor development is unknown. Thus, we analyzed the symmetry of cell fates by monitoring cell-type specification in sister cells emerging after cell division (Figure S2H). In control conditions, sister cell fates predominantly exhibited symmetry, with less than 5% showing asymmetry, which is comparable to what occurs in non-transformed intestine[48] (Figure 2I). Strikingly, lactate increased the frequency of asymmetric cell fates to 18.3% (Figure 2I). Asymmetric events predominantly consisted in one of the sister cells dedifferentiating (Figure S2I), suggesting that the process of cell division can be regulatory of cell fate. Altogether these findings indicate that lactate induces CSCs by inhibiting differentiation and, importantly, by inducing CDCs to regress to a proliferative CSCs state. These observations reveal an important role for elevated lactate levels, characteristic of the Warburg effect, on the regulation of tumor development.

Lactate rewires metabolism and induces stemness independently of mitochondria pyruvate import

To elucidate the mechanism underlying lactate-induced stemness, we analyzed its impact on the metabolome. Lactate, in conjunction with low glucose, decreased the levels of glycolytic intermediates while increasing tricarboxylic acid cycle (TCA) intermediates, suggesting increased mitochondrial activity (Figures 3A and 3B). Pyruvate and acetyl-coenzyme A (CoA) levels were significantly increased, implying the metabolization of lactate to pyruvate and subsequently to acetyl-CoA (Figures 3A, 3B, and S3A). Consistent with lactate treatment, pyruvate increased acetyl-CoA levels and increased the number of CSCs, with a similar increase in CSCs also observed upon LDHA inhibition (Figures 3C, S3B, S3C, and S3AG). Furthermore, dichloroacetate (DCA), which inhibits pyruvate dehydrogenase kinase (PDK) thereby activating pyruvate dehydrogenase (PDH), increased acetyl-CoA levels, and mitochondrial pyruvate oxidation (Figures S3D–S3H). In agreement with previous, DCA increased the expression of stem cell markers and of CSC numbers (Figures 3C, 3D, S3B, and S3I), a phenotype also observed when treating with VER-246608,[50] an ATP-competitive inhibitor of PDK (PDK1,2,3, and 4) (Figures S3J and S3K). Live imaging coupled to CellPhenTracker revealed that DCA recapitulates the effect of lactate: it inhibited cell differentiation, enhanced dedifferentiation and induced asymmetric cell fates, prolonged cell-cycle duration, and increased the number of cycling clones (Figures 3E, 3F, and S3L–S3N). Thus, PDH activation, similar to lactate, increased respiration, pyruvate and acetyl-CoA levels, and recapitulated lactate's effects on tumor developmental dynamics.

Prior studies from others and us showed that intestinal stem cells exhibit a higher abundance of mitochondria and elevated mitochondrial activity.[14,51,52] We therefore examined whether lactate- and DCA-induced stemness depends on mitochondrial function. Organoids grown on lactate showed increased mitochondrial respiration and its inhibition compromised viability, indicating a dependency on mitochondria under these conditions (Figures 3G, S3O, S3P, and S3S). Upon DCA treatment, mitochondrial inhibition rescued the increase in CSCs, showing dependency on mitochondria in inducing stemness (Figures 3H, S3Q, S3R, S3T, and S3U). Next, we inhibited the mitochondrial pyruvate carrier (MPC) with UK-5099, hypothesizing that blocking pyruvate import might prevent CSC increase. Unexpectedly, MPC inhibition did not reverse the increase in CSC induced by lactate, pyruvate, DCA, or VER-246608 (Figures 3I and S3V–S3Z). We further analyzed mitochondrial respiration upon MPC inhibition and observed a decrease in basal and maximal respiration with short-term UK-5099 treatment (1 h) (Figure S3AA). Notably, after long-term inhibition (3 days) basal respiration was restored and became sensitive to glutamine and fatty acid oxidation inhibition (Figures S3AA–S3AC), indicating that tumor organoids are metabolically flexible as they can adapt to oxidize alternative substrates to pyruvate to sustain mitochondrial activity, while there is dependency on pyruvate for maximal respiration. In lactate-grown organoids, basal respiration was unaffected by inhibition of MPC, glutamine and fatty acid oxidation inhibition, or by the combination of all three (Figure S3AD). Lactate can enter mitochondria and support OXPHOS by mechanisms still under investigation.[53] We performed a time course Seahorse analysis of mitochondrial respiration by first depriving organoids of glucose and lactate followed by adding one or the other as substrates. Lactate addition indeed increased oxygen consumption, and this was not affected by MPC inhibition, indicating that indeed lactate serves as a substrate for mitochondrial respiration independently of its conversion to pyruvate in the cytosol (Figure 3J). Notably in response to glucose, glycolysis increased while respiration was inhibited, a seemingly transient response to glucose deprivation, as this was not observed in non-glucose-deprived control organoids (Figures 3J, 3K, S3AE, and S3AF). Collectively, these results show that lactate drives metabolic remodeling, increasing mitochondrial respiration, TCA cycle intermediates, pyruvate and acetyl-CoA. Moreover, mitochondrial activity is required for inducing cancer stemness. We next investigated whether lactate-induced metabolic remodeling could regulate stemness through mechanisms beyond bioenergetics elsewhere in the cell.

Lactate enhances histone acetylation and chromatin accessibility at the *MYC* locus

Transcriptional reprogramming plays a pivotal role in regulating cell-type specification.[54–56] RNA sequencing analysis on tumor

---

(I) FACS analysis of STAR-based CSC percentages in TPO3 grown in control (Ctrl) or in lactate (Lact) conditions for 5 days, with or without 10 μM UK-5099 (n = 3, one-way ANOVA).

(J and K) Oxygen consumption rate (OCR) and extracellular acidification rate (ECAR) of glucose-deprived TPO3 upon D-glucose (12 mM) or L-lactate (24 mM) injection with or without pre-treatment of 10 μM UK-5099 (UK) (representative experiment, n = 4). The glucose-free medium was supplemented with glutamine, pyruvate, and B27.

In (A)–(D), (G), and (I), control refers to 12 mM glucose, lactate refers to 23 mM lactate + 0.5 mM glucose, and pyruvate refers to 23 mM pyruvate + 0.5 mM glucose. In (B), (C), and (G)–(K), data are presented as mean ± SEM. (ns: non-significant).

See also Data S1 and Figure S3.
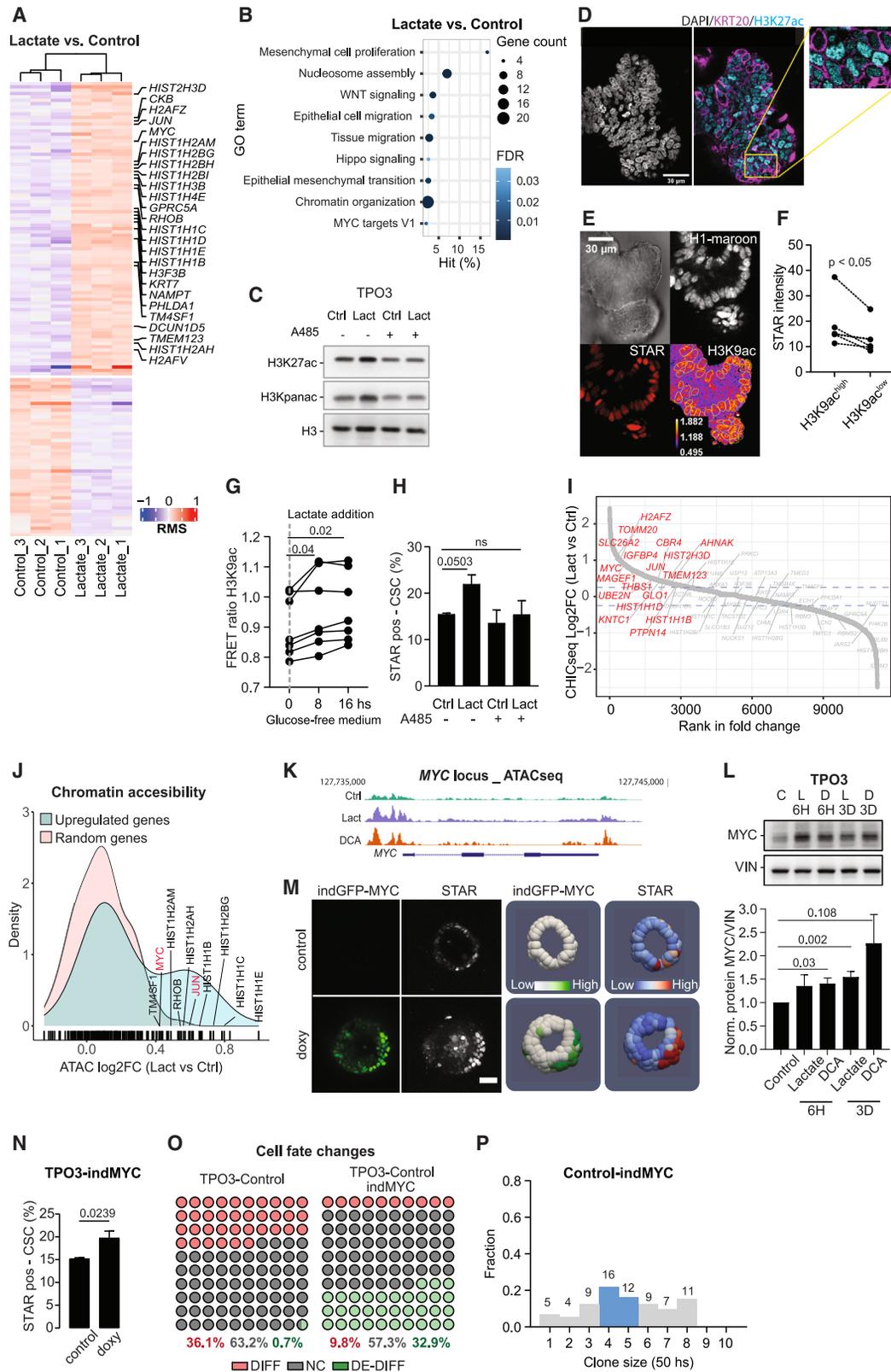
organoids revealed significant changes in the expression of 134 genes upon lactate treatment (Figure 4A). Pathway enrichment analysis showed enrichment in WNT signaling, cell proliferation, migration, and notably, various categories associated with chromatin remodeling (Figure 4B). Interestingly, similar results were observed when treated with DCA (Figures S4A and S4B). Chromatin remodelers are tightly regulated by the availability of their substrates and cofactors.[57] Thus, elevated acetyl-CoA levels, observed following lactate, pyruvate, and DCA treatments (Figures 3A, 3B, S3A, S3C, S3E, and S3F), could potentially enhance histone acetylation and chromatin accessibility, thereby influencing transcription. Aligned with that, lactate, pyruvate, and DCA increased histone acetylation at several residues (H3pan, H3K27, H3K9) (Figures 4C and S4C–S4G), and this effect was a consequence of acetyltransferase activity, as it was sensitive to p300/CBP inhibition by A485 (Figures 4C and S4C–S4E). Notably, adding lactate, pyruvate, or acetate to glucose-containing control medium increased both the number of CSCs and histone acetylation (Figures S4H–S4L), suggesting that acetyl-CoA availability limits histone acetylation.

Immunofluorescence analysis showed that CDCs (KRT20-positive) exhibit lower levels of histone acetylation compared with KRT20-negative cells, both in tumor organoids and in tumor tissue, suggesting increased acetylation in CSCs (Figures 4D and S4M–S4O). To further investigate this, we utilized an H3K9ac FRET reporter[58] validated in organoids (Figures S4P–S4R). Cell-type FRET confirmed higher acetylation levels in CSCs compared with CDCs (Figures 4E, 4F, and S4S–S4U), corroborated by western blot analysis (Figures S4V and S4W). To delve deeper into lactate's impact on acetylation, we deprived organoids of glucose, followed by lactate addition, and analyzed the cell-type response on the H3K9ac reporter. Both CSCs and CDCs increased acetylation upon lactate

(Figures 4G and S4X), suggesting that lactate-driven increased acetylation in CDCs could mediate dedifferentiation. Consistent with this, inhibition of histone acetylation counteracted the effect of lactate and DCA in increasing CSCs (Figures 4H and S4Y–S4AA), reinforcing the idea that lactate induces CSC identity through epigenetic remodeling.

Next, we investigated changes in histone acetylation for genes differentially expressed upon lactate treatment. Chromatin ImmunoCleavage (ChIC) revealed increased H3K27 acetylation at the promoter regions (transcription start site [TSS] ± 2 kb) of some upregulated genes, including MYC, JUN, and several histone genes (Figure 4I). To assess the impact of histone acetylation on chromatin accessibility, we performed assay for transposase-accessible chromatin using sequencing (ATAC) (Figure S4AB). ATAC analysis showed that lactate altered chromatin accessibility in 652 genes, with ninety percent of them showing increased accessibility and the remaining ten percent showing reduced accessibility (Figure S4AB). Subsequently, we assessed whether significantly upregulated genes upon lactate treatment displayed differential chromatin accessibility. Randomly selected genes showed a normal distribution in changes in chromatin accessibility upon lactate (Figure 4J). However, lactate upregulated genes showed a distinct distribution with a subset showing increased accessibility (Figure 4J). Notably, genes in this subset included histones and oncogenes such as MYC and JUN (Figures 4J, 4K, and S4AB), transcription factors of the WNT pathway that regulate stemness, proliferation and migration in CRC.[59–64] Consistently, increased H3K27ac and chromatin accessibility were also found in MYC upon DCA treatment (Figures 4K, S4AB, and S4AC), and both lactate and DCA increased MYC protein levels (Figure 4L). Furthermore, inhibiting MCT transporters, which increases the number of CSCs (Figure S2D), augmented intracellular acetyl-CoA and

---

Figure 4. Lactate enhances histone acetylation and chromatin accessibility at the MYC locus

(A) Analysis of gene expression (RNA-seq) of TPO3 upon lactate vs. control (genes with false discovery rate [FDR] < 0.05 are shown).

(B) Gene Ontology (GO) enrichment analysis on upregulated genes in TPO3 lactate vs. control (ShinyGO, FDR < 0.05). See Table S7 for additional significant pathways.

(C) Effect of lactate and A485 (2 μM, 3 and 4 h, respectively) on histone acetylation by western blot ($n = 4$–9).

(D) Representative immunostaining images of TPO3 organoids ($n = 3$) stained for KRT20 and H3K27ac. DAPI was used to label nuclei (scale bar, 30 μm).

(E) Live imaging of H3K9ac FRET in TPO4 CSCs and CDCs (scale bar, 30 μm).

(F) Comparison of mean STAR intensity values between H3K9ac[high] and H3K9ac^{low} cells ($n = 6$, paired t test). H3K9ac FRET was measured in nuclear fraction.

(G) Single-cell quantification of nuclear H3K9ac FRET at the start (0 h), 8, and 16 h after the addition of 10 mM lactate to TPO3 organoids pre-treated with glucose-free medium for 3 h ($n = 7$ organoids, Dunnett's multiple comparisons test).

(H) FACS analysis of STAR-based CSC percentages in TPO3 after 5 days of culture under control or lactate conditions with or without A485 (0.5 or 2 μM, adjusted according to inhibitor batches) (mean ± SEM, $n = 6$, Dunnett's multiple comparisons test).

(I) Changes in H3K27ac ChIC signal (TSS ± 2 kb) in TPO3 organoids cultured in lactate vs. control (7 h). Displayed genes are significantly upregulated in RNA-seq analysis (refer to A). Red = genes with log$_2$ fold change (log$_2$FC) values $\geq$ 0.3.

(J) Distribution of chromatin accessibility changes (ATAC log$_2$FC) between groups of random genes ($n = 97$) and upregulated genes ($n = 95$) in RNA-seq analysis of lactate vs. control organoids (Wilcoxon test). Upregulated genes with a log$_2$FC > 0.33 are displayed.

(K) Zoom-in of MYC locus for normalized ATAC peak signals in control, lactate, and DCA samples (Genome Browser, http://genome.ucsc.edu/).

(L) MYC expression in TPO3 after 6 h or 3 days of culture in lactate (L6H and L3D) or treatment with 20 mM DCA (D6H and D3D) compared with control (C) organoids. Vinculin (VIN) serves as loading control (mean ± SEM, 6H: $n = 5$ for both treatments, 3D: lactate $n = 9$, DCA $n = 5$, one-sample t test).

(M and N) Representative images of TPO3 indGFP-MYC STAR-NLS organoids with and without doxycycline (doxy, 40 h, scale bar, 50 μm) and (N) quantification of stem cell numbers by flow cytometry after 3 or 5 days of doxy treatment ($n = 8$, paired t test). Digital reconstruction was generated using Paraview.

(O) Percentages of cell fate changes: differentiation (DIFF), dedifferentiation (DEDIFF), and no change (NC) during TPO3 development in control conditions ($n = 7$, same plot as the control condition in Figure 2E) or with inducible MYC (indMYC, $n = 3$) (mean, Sidak's multiple comparisons test, p value of control vs. control-indMYC DIFF: 0.0208, DEDIFF: 0.042, and NC: 0.88).

(P) Clone size distributions of all lineages of TPO3 with inducible MYC ($n = 2$). Each lineage tree was recorded for a minimum of 50 h. Control values are shown in Figure 2H.

In (A), (B), (C), and (H)–(L), control refers to 12 mM glucose, and lactate refers to 23 mM lactate + 0.5 mM glucose. (ns: non-significant).

See also Data S1, Table S7, and Figure S4.

MYC protein levels (Figures S4AD–S4AF), revealing that endogenous lactate production regulates MYC. Next, we used a doxycycline inducible MYC expression system, which showed that MYC induction is sufficient to increase the population of CSC, inhibit differentiation, activate dedifferentiation and increase clone sizes (Figures 4M–4P and S4AG–S4AJ). These findings suggest that lactate's regulation of stemness relies on the epigenetic regulation of MYC expression.

Lactate-induced stemness and plasticity is MYC dependent

Next, we analyzed publicly available RNA datasets from two independent studies, comprising 290 and 96 tumors, respectively.[65,66] For each tumor, we calculated the scores for previously reported transcriptional signatures of MYC, metabolic pathways, and cell signaling (Table S6),[52,67,68] by sample-wise scoring using single-sample gene set enrichment analysis (ssGSEA).[69] This analysis at the tumor level, revealed a strong positive correlation between the MYC signature and both glycolytic and OXPHOS scores (Figures S5A and S5B), consistent with previous studies.[70,71] This finding led us to investigate the metabolic state of those tumor cells with a high MYC signature. At the single-cell level, MYC signature score was variable across cell types (Figure 5A). This was confirmed by immunostaining of tumor biopsies, which showed variable MYC levels even when β-catenin, its main upstream regulator,[61] was homogeneously expressed across cells (Figure S5C). At the single-cell level, the MYC signature positively correlated with proliferation and mitochondrial metabolism (Figures 5A, 5B, S5D, and S5E). Notably, TA-like tumor cells showed the highest scores for these three signatures (Figures 5B and S5E). In contrast to bulk analysis, MYC signatures at the single-cell level did not correlate with glycolytic signatures; instead, higher glycolytic scores were observed in CDCs, consistent with findings in organoids (Figures 1C, 5A, 5C, S1G, S5D, and S5E). These patterns were robustly observed in 57 tumors and were not a consequence of shared genes in the signatures, as there is minimal gene overlap between them (Figure S5F). These gene expression analyses align with our organoid findings, showing that lactate induces a "MYC-on" state. Thus, glycolytic CDCs and other non-epithelial glycolytic cells in the tumor microenvironment may create a high-lactate environment supporting a MYC-on program, promoting the occurrence of oxidative, proliferative CSCs *in vivo*.

The effect of lactate on MYC expression and, consequently, on stemness seems to be epigenetically regulated. BRD4, an epigenetic reader recognizing acetylated lysine residues, activates the transcription of various genes, including *MYC*.[72–74] Given BRD4's critical role in MYC expression in human cancers, bromodomain and extra terminal domain (BET) inhibitors have been investigated as a potential anticancer therapy.[72,74] RNA sequencing analysis of organoids treated with BRD4 inhibitors at concentrations that did not affect viability, revealed altered expression of several genes, predominantly inhibiting the expression of *MYC* and MYC-signature genes (Figures S5G–S5I). Notably, BRD4 inhibition (JQ1 and IBET762) prevented the effect of lactate and DCA on increasing the CSC population (Figures 5D, S5J, and S5K). Next, we performed 4D live imaging coupled with CellPhenTracker to examine the impact of BRD4 inhibition on lactate-mediated regulation of cell plasticity. Remarkably, while

BRD4 inhibition partially rescued lactate-induced repression of differentiation, it drastically prevented lactate-driven dedifferentiation to the CSC state (Figures 2E, 5G, and 5H). Notably, the treatment also reverted asymmetric cell divisions, suggesting a mechanistic interdependency between these two events (Figures 2I and 5F). Unexpectedly BRD4 inhibition also prevented the prolonged cell-cycle length induced by lactate, suggesting that this effect may not attributed to metabolic restriction (Figure S5L). To further evaluate MYC as a downstream effector of lactate, we used a MYC inhibitor[75] and generated a doxycycline inducible MYC knockdown line (Figures S5M–S5O). MYC inhibitor significantly, though partially, reversed the lactate-induced increase in CSCs and rescued the occurrence of dedifferentiation events (Figures 2E, 5E, 5G, and 5I). Similarly, the knockdown of MYC partially reverted the increase in CSCs and rescued dedifferentiation (Figures 2E, S5P, and S5Q). Furthermore, both strategies reduced the frequency of asymmetric cell fates and decreased the clone size, while the cell-cycle length was further extended (Figures 5F, S5L, and S5R–S5V), reflecting MYC's role in regulation of proliferation. Lastly, inducing MYC expression in lactate-grown organoids showed an additive, albeit not significant, increase of CSCs (Figures S5W and S5X). This observation, along with the partial reversion of the phenotype by MYC inhibition and knockdown, may suggest the existence of additional mechanism beyond MYC and downstream of lactate. Collectively, these findings reveal that lactate, through epigenetic regulation, influences key aspects of tumor development, including proliferation, stemness, and cancer cell plasticity.

DISCUSSION

Cancers exhibit genetic and phenotypic heterogeneity, which is linked to poor patient outcomes in various clinical contexts.[76–78] Despite this, our understanding on how tumor hierarchical organization and tumor cell interactions contribute to tumor development, therapy resistance, and metastatic dissemination remains limited.[79–81]

Lactate, whose abundant production is a hallmark of cancer, has profound effects on tumor development by regulating angiogenesis, promoting immunosurveillance, and supporting metastasis.[82–86] In this study, CellPhenTracker imaging analysis disclosed that while both CSCs and CDCs perform glycolysis and mitochondrial respiration, lactate is more abundantly produced by CDCs, and CSCs are more prompt to uptake the metabolite. Importantly, lactate acts as an intrinsic regulator of tumor dynamics by increasing CSC numbers through halting their differentiation and by inducing CDCs to revert to a proliferative CSC state. The higher glycolytic activity in CDCs is not due to mitochondrial dysfunction or hypoxic conditions (Figures 1I, S1Z, and S1AA). The directionality of lactate transport is primarily defined by the metabolite gradient across the cell membrane[87,88] rather than by differential expression of the MCT transporters. In agreement, CSCs, which maintain lower basal lactate levels, show a higher capacity for lactate uptake. Lower lactate levels in CSCs are likely maintained by their reduced lactate production and by lactate serving as a substrate for CSCs' elevated mitochondrial activity.

Mechanistically lactate increases TCA cycle metabolites, pyruvate, acetyl-CoA, and mitochondrial respiration. Mitochondrial
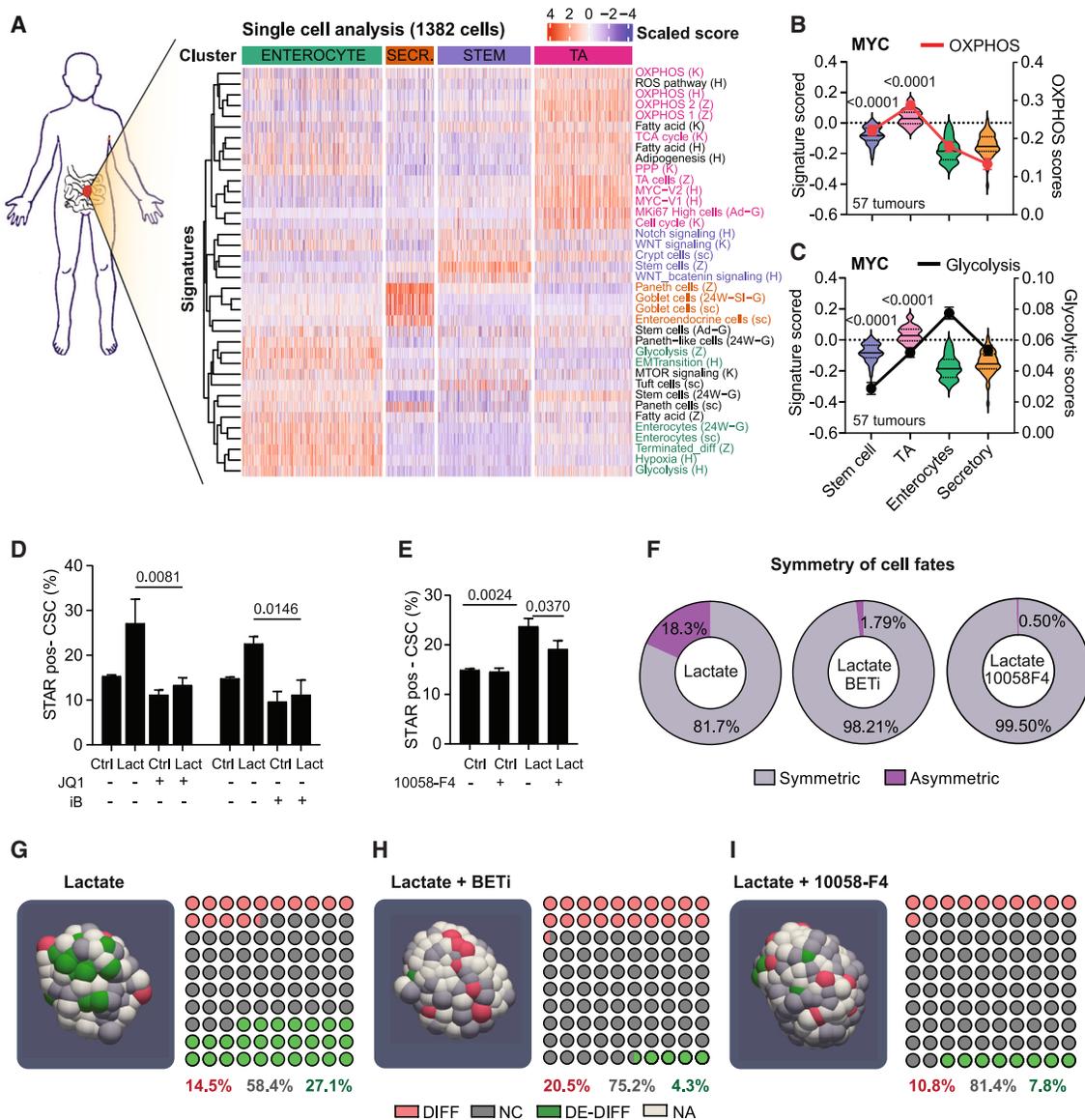
Figure 5. Lactate-induced stemness and plasticity is MYC dependent

(A) Representative heatmap of signature scores for epithelial cancer cell types (*KRT8*+*EPCAM*+, GEO: GSE161277, P1_carcinoma tumor).

(B and C) Comparison of mean scores of MYC-V2 to glycolysis and OXPHOS signatures in the different cell types derived from 57 scRNA-seq datasets of human CRC tumors.

(D and E) FACS analysis of STAR-based CSC percentages in TPO3 grown for 5 days in control (Ctrl) or lactate (Lact) conditions with and without (D) JQ1 (100 nM, 5 days, *n* = 6) or IBET762 (iB, 500 nM, 5 days, *n* = 3) or with and without (E) MYC-MAX inhibitor 10058-F4 (500 nM, 48 h, *n* = 9).

(F) Quantification of cell fate symmetry between sister-pairs in TPO3 cultured in lactate (*n* = 4, same as in Figure 2I), or in combination with JQ1 (100 nM, lactate + BETi, *n* = 3), or with 10058-F4 (500 nM, lactate + 10058-F4, *n* = 3) (*p* value lactate vs. lactate+BETi 0.0024, lactate vs. lactate+10058F4 0.0016). Control values are shown in Figure 2I.

(G–I) Quantification of cell fate changes and digital reconstruction of representative organoids cultured in lactate (*n* = 4, same plot as the lactate condition in Figure 2E), or in combination with JQ1 (100 nM, lactate + BETi, *n* = 3), or with 10058-F4 (500 nM, lactate + 10058-F4, *n* = 3). Details of the analyzed organoids are in Table S2. Pink, green, and gray represent differentiation (DIFF), dedifferentiation (DEDIFF), or no change (NC), respectively. White cells: undefined (*p* value DEDIFF: lactate vs. lactate+BETi 0.0209, lactate vs. lactate+10058F4 0.0525). Control values are shown in Figure 2E.

In (A)–(C), signature details can be found in Table S6. In (D)–(I), control refers to 12 mM glucose, and lactate refers to 23 mM lactate + 0.5 mM glucose. In (B)–(E), data were presented as mean ± SEM. Tukey's multiple comparisons test for (B), (C), and (E), and Dunnett's multiple comparisons test for (D) and (F)–(I). (ns: non-significant).

See also Data S1 and Figure S5.

activity was showed to be required for inducing CSC identity, but blocking pyruvate transport into mitochondria did not rescue the increase in CSCs by lactate or DCA. On one hand, lactate can support mitochondrial activity independently of its conversion to pyruvate in the cytosol; on the other hand, lactate- and DCA-driven increases in acetyl-CoA levels may occur independently of mitochondria, potentially via nuclear PDH activity, as reported by others.[89] In this context, the dependency of CSC identity on mitochondrial function may also rely on ATP production and/or mitochondrial redox regulation of cell signaling, as shown in mouse intestinal stem cells, where mitochondrial activity induces mitogen-activated protein kinase (MAPK) p38 phosphorylation.[14] Here, lactate-induced respiration persists despite simultaneous inhibition of pyruvate import, glutamine, and fatty acid oxidation, supporting lactate's role as a mitochondrial substrate. Determining the precise metabolic pathway from lactate to the rise in acetyl-CoA levels warrants further investigation.

Integrative analysis of chromatin accessibility and gene expression pointed at histones, JUN, and MYC as potential regulators of lactate-induced phenotypes. Notably, the *MYC* locus is metabolically sensitive through lactate-driven histone acetylation in a BRD4-dependent manner. We found that BRD4 activity is required for lactate-induced dedifferentiation into the CSC state, consistent with studies showing that BRD4 inhibition slows down CRC tumor growth and reduces liver metastasis in mice.[90,91] MYC inhibition and silencing partially reversed the lactate-driven CSC increase, possibly due to insufficient inhibitor efficacy and incomplete knockdown. On the other hand, MYC induction alone is sufficient to mimic lactate-induced phenotype. Additional mechanisms beyond MYC may act downstream lactate. MYC induction in lactate-grown tumor organoids led to an additive increase in CSCs, suggesting that lactate may act through other epigenetic targets, acetylation of non-histone proteins, or mitochondrial activity-related signals. Lactate can also bind the hydroxycarboxylic acid receptor (HCAR) triggering a myriad of responses in cancer cells.[92,93] CSCs are induced not only by exogenous lactate but also by endogenous lactate production, as evidenced by MCT inhibition, suggesting HCAR-independent mechanisms. Furthermore, lactate serves as a substrate for histone lactylation, a modification that similarly to acetylation, seems to activate transcription.[94] Thus, lactate may induce lactylation of histones and non-histone proteins, an aspect yet to be investigated.

Lactate-induced histone acetylation and increased CSC numbers were observed in both tumor organoid lines in this study, despite that some differences between these lines were identified. Low glucose decrease the acetyl-CoA pool and CSC numbers in TPO3, while in TPO4 neither is affected (Figures S2B and S2L), suggesting a role for SMAD4 loss in TPO4 in increasing metabolic flexibility. Interestingly, we found that TPO4 exhibited higher MYC expression, increased stem cell marker genes, and a higher number of CSCs (Figures S2J, S2K, S5Y, and S5Z). Imaging analysis also revealed more frequent dedifferentiation events in TPO4 compared with TPO3 (Figure S5P), linking MYC levels with cellular plasticity. Consistent with these observations, SMAD4 loss was shown to enhance WNT signaling in APC-mutated colon cell lines and to reactivate WNT signaling in enterocytes, leading to ectopic crypt formation.[95–97] Furthermore, orthotopic transplantation of TPOs demonstrates metastatic capacity in TPO4.[9] TPO4 showed

higher resistance to BET inhibitors, potentially associated with elevated MYC and WNT signaling activities in this line.

Lactate promotes proliferative CSCs with longer cell cycles, leading to increased numbers of cycling clones within the tumors, which can impact the efficacy of conventional anticancer therapy targeting cycling cells. While precision medicine advances, conventional chemotherapies continue to serve as the workhorse of oncology. Our findings reveal lactate's role in supporting CSC identity by inducing dedifferentiation, contributing to the mechanistic understanding of tumor resistance and relapse. The use of BET inhibitors for cancer treatment is limited by their toxicity.[72,98] Our findings suggest that a lower dose of BET inhibitors could prevent tumor relapse by inhibiting therapy-surviving cancer cells from regressing to a proliferative CSC state via MYC activation. A more thorough mechanistic understanding of how tumor hierarchical and metabolic organization contributes to tumor initiation, development, and metastasis will ultimately enable the development of more effective therapeutic strategies against cancer.

Limitations of the study

We utilized TPO3 and TPO4 organoids as tumor models. In TPO3, rotenone and oligomycin reversed the increase in CSCs when DCA was administered first, followed by the inhibitors. However, in TPO4, the phenotype was reversed only when adding the inhibitors simultaneously (Figures S3U and S3AH), indicating that inhibiting mitochondria activity can prevent the increment of CSCs in TPO4 but is less effective once the phenotype is established. A deeper molecular understanding of the metabolic differences triggered by SMAD4 mutation requires further investigation. We constructed inducible lines for MYC knockdown using short hairpin RNAs. At early organoid passage numbers, shMYC expression resulted in a partial but significant decrease in the number of CSCs induced by lactate. Imaging analyses of this line were done at early organoid passage numbers. However, at later passage numbers, this phenotype became less robust, seemingly due to the negative selection toward the knockdown of MYC. In agreement, constitutive MYC knockdown resulted in cell death (not shown). BET inhibitors reversed the increase in CSCs by lactate in both lines. Due to time restrictions, the effects of shMYC and MYC inhibition on CSC induction by lactate were assessed in TPO3 only. LDHA inhibition (GSK2837808A) effectively decreased glycolysis, increased mitochondrial respiration (Figures S5AA and S5AB), and increased the number of CSCs in TPO3. However, we did not observe an increase in acetyl-CoA levels or histone acetylation (not shown), suggesting alternative metabolically driven mechanisms at play. Laconic-NLS and H2B-SoNar are localized and measured in the nucleus, which is readily compatible with 3D single-cell tracking. Their metabolic response was comparable to their cytosolic counterparts, as analyzed in validation experiments using metabolites or inhibitors (not shown).

RESOURCE AVAILABILITY

Lead contact

Further information and requests for resources and reagents should be directed to and will be fulfilled by the lead contact, M.J. Rodríguez Colman (m.j.rodriguezcolman@umcutrecht.nl).

Materials availability

Upon reasonable request, plasmids generated in this study can be provided via lead contact.

Data and code availability

- Metabolomics data have been deposited at MetaboLights: MTBLS11849.
- Unprocessed source data underlying all plots and graphs are available in Data S1.
- Sequencing data for RNA, ATAC, ChIC have been deposited in the EGA European Genome-Phenome Archive under the accession number: EGA: EGAS50000000063.
- Any additional information required to reanalyze the data reported in this paper is available from the lead contact upon request.

AUTHOR CONTRIBUTIONS

Conceptualization, M.J.R.C. and N.T.B.N.; methodology and investigation, M.J.R.C., N.T.B.N., S.G., M.C.L., and R.N.U.K.; metabolomics, C.G., E.C.A.S., and B.M.T.B.; TPO organoid model, J.D., H.C., and M.V.; RNA and ATAC sequencing, N.T.B.N., H.N., and M.V.; imaging analysis, N.T.B.N., N.A., R.N.U.K., M.A.B., S.J.T., and J.S.v.Z.; patient material – tissue slides, Y.V.; manuscript writing, M.J.R.C. and N.T.B.N.; manuscript reviewing, M.J.R.C., N.T.B.N, B.M.T.B., M.V., S.J.T., J.D., L.M.B., and R.N.U.K.; funding acquisition, B.M.T.B. and M.J.R.C.

DECLARATION OF INTERESTS

H.C. is inventor on patents related to organoid research. His full disclosure: www.uu.nl/staff/JCClevers/Additional functions.

DECLARATION OF GENERATIVE AI AND AI-ASSISTED TECHNOLOGIES IN THE WRITING PROCESS

During the preparation of this work, the authors used ChatGPT-4 cautiously to verify the readability of long sentences. After using this tool, the authors reviewed and edited the content as needed and take full responsibility for the content of the publication.

STAR★METHODS

Detailed methods are provided in the online version of this paper and include the following:

- KEY RESOURCES TABLE
- EXPERIMENTAL MODEL AND STUDY PARTICIPANT DETAILS
- METHOD DETAILS
  - Cloning
  - Lentiviral transduction
  - FACS sorting
  - Immunofluorescent (IF) staining in organoids
  - Immunohistochemistry (IHC) staining
  - Mitochondrial live imaging
  - Live imaging of organoids
  - Paraview rendering
  - Validation of biosensors
  - RNA extraction and real-time PCR
  - Flow cytometry
  - Protein lysates and western blot
  - Metabolomics
  - Seahorse XF Flux
  - bulkChICseq sample preparation
  - ATACseq sample preparation and pre-processing
  - RNAseq sample preparation
- QUANTIFICATION AND STATISTICAL ANALYSIS
  - Imaging analysis of fixed stains
  - Single-cell analysis of organoid growth
  - Single-cell analysis of metabolic dynamics
  - Single-cell analysis of H3K9ac
  - scRNAseq analysis
  - Microarray sample signature scoring
  - Real-time PCR analysis
  - Metabolomics analysis
  - Seahorse analysis
  - bulkCHICseq data preprocessing and analysis
  - ATACseq analysis
  - RNAseq analysis
  - Gene ontology analysis of sequencing data
  - Statistical Analysis

SUPPLEMENTAL INFORMATION

Supplemental information can be found online at https://doi.org/10.1016/j.cmet.2025.01.002.

REFERENCES

1. Alzahrani, S.M., Al Doghaither, H.A., and Al-Ghafari, A.B. (2021). General insight into cancer: an overview of colorectal cancer (Review). Mol. Clin. Oncol. *15*, 271. https://doi.org/10.3892/mco.2021.2433.

2. Barker, N., van Es, J.H., Kuipers, J., Kujala, P., van den Born, M., Cozijnsen, M., Haegebarth, A., Korving, J., Begthel, H., Peters, P.J., et al. (2007). Identification of stem cells in small intestine and colon by marker gene Lgr5. Nature *449*, 1003–1007. https://doi.org/10.1038/nature06196.

3. Mah, A.T., Yan, K.S., and Kuo, C.J. (2016). Wnt pathway regulation of intestinal stem cells. J. Physiol. *594*, 4837–4847. https://doi.org/10.1113/JP271754.

4. Novellasdemunt, L., Antas, P., and Li, V.S.W. (2015). Targeting Wnt signaling in colorectal cancer. A Review in the Theme: Cell Signaling: Proteins, Pathways and Mechanisms. Am. J. Physiol. Cell Physiol. *309*, C511–C521. https://doi.org/10.1152/ajpcell.00117.2015.

5. Schepers, A.G., Snippert, H.J., Stange, D.E., van den Born, M., van Es, J.H., van de Wetering, M., and Clevers, H. (2012). Lineage tracing reveals Lgr5+ stem cell activity in mouse intestinal adenomas. Science *337*, 730–735.

6. Shimokawa, M., Ohta, Y., Nishikori, S., Matano, M., Takano, A., Fujii, M., Date, S., Sugimoto, S., Kanai, T., and Sato, T. (2017). Visualization and targeting of LGR5(+) human colon cancer stem cells. Nature *545*, 187–192. https://doi.org/10.1038/nature22081.

7. Humphries, A., Cereser, B., Gay, L.J., Miller, D.S.J., Das, B., Gutteridge, A., Elia, G., Nye, E., Jeffery, R., Poulsom, R., et al. (2013). Lineage tracing reveals multipotent stem cells maintain human adenomas and the pattern of clonal expansion in tumor evolution. Proc. Natl. Acad. Sci. USA *110*, E2490–E2499. https://doi.org/10.1073/pnas.1220353110.

8. de Sousa, Melo, F., Kurtova, A.V., Harnoss, J.M., Kljavin, N., Hoeck, J.D., Hung, J., et al. (2017). A distinct role for Lgr5(+) stem cells in primary and metastatic colon cancer. Nature *543*, 676–680. https://doi.org/10.1038/nature21713.

9. Fumagalli, A., Drost, J., Suijkerbuijk, S.J.E., van Boxtel, R., de Ligt, J., Offerhaus, G.J., Begthel, H., Beerling, E., Tan, E.H., Sansom, O.J., et al. (2017). Genetic dissection of colorectal cancer progression by orthotopic transplantation of engineered cancer organoids. Proc. Natl. Acad. Sci. USA *114*, E2357–E2364. https://doi.org/10.1073/pnas.1701219114.

10. Heinz, M.C., Peters, N.A., Oost, K.C., Lindeboom, R.G.H., van Voorthuijsen, L., Fumagalli, A., van der Net, M.C., de Medeiros, G., Hageman, J.H., Verlaan-Klink, I., et al. (2022). Liver colonization by colorectal cancer metastases requires YAP-controlled plasticity at the micrometastatic Stage. Cancer Res. *82*, 1953–1968. https://doi.org/10.1158/0008-5472.CAN-21-0933.

11. Cortina, C., Turon, G., Stork, D., Hernando-Momblona, X., Sevillano, M., Aguilera, M., Tosi, S., Merlos-Suárez, A., Stephan-Otto Attolini, C., Sancho, E., et al. (2017). A genome editing approach to study cancer stem cells in human tumors. EMBO Mol. Med. *9*, 869–879. https://doi.org/10.15252/emmm.201707550.

12. Greenbaum, A., Martin, D.R., Bocklage, T., Lee, J.H., Ness, S.A., and Rajput, A. (2019). Tumor heterogeneity as a predictor of response to neoadjuvant chemotherapy in locally advanced rectal cancer. Clin. Colorectal Cancer *18*, 102–109. https://doi.org/10.1016/j.clcc.2019.02.003.

13. Punt, C.J.A., Koopman, M., and Vermeulen, L. (2017). From tumour heterogeneity to advances in precision treatment of colorectal cancer. Nat. Rev. Clin. Oncol. *14*, 235–246. https://doi.org/10.1038/nrclinonc.2016.171.

14. Rodríguez-Colman, M.J., Schewe, M., Meerlo, M., Stigter, E., Gerrits, J., Pras-Raves, M., Sacchetti, A., Hornsveld, M., Oost, K.C., Snippert, H.J., et al. (2017). Interplay between metabolic identities in the intestinal crypt supports stem cell function. Nature *543*, 424–427. https://doi.org/10.1038/nature21673.

15. Beyaz, S., Mana, M.D., Roper, J., Kedrin, D., Saadatpour, A., Hong, S.J., Bauer-Rowe, K.E., Xifaras, M.E., Akkad, A., Arias, E., et al. (2016). High-fat diet enhances stemness and tumorigenicity of intestinal progenitors. Nature *531*, 53–58. https://doi.org/10.1038/nature17173.

16. Bruens, L., Ellenbroek, S.I.J., Suijkerbuijk, S.J.E., Azkanaz, M., Hale, A.J., Toonen, P., Flanagan, D.J., Sansom, O.J., Snippert, H.J., and van Rheenen, J. (2020). Calorie restriction increases the number of competing stem cells and decreases mutation retention in the intestine. Cell Rep. *32*, 107937. https://doi.org/10.1016/j.celrep.2020.107937.

17. Ludikhuize, M.C., Meerlo, M., Gallego, M.P., Xanthakis, D., Burgaya Julià, M., Nguyen, N.T.B., Brombacher, E.C., Liv, N., Maurice, M.M., Paik, J.H., et al. (2020). Mitochondria define intestinal stem cell differentiation downstream of a FOXO/Notch axis. Cell Metab. *32*, 889–900.e7. https://doi.org/10.1016/j.cmet.2020.10.005.

18. Schell, J.C., Wisidagama, D.R., Bensard, C., Zhao, H., Wei, P., Tanner, J., Flores, A., Mohlman, J., Sorensen, L.K., Earl, C.S., et al. (2017). Control of intestinal stem cell function and proliferation by mitochondrial pyruvate metabolism. Nat. Cell Biol. *19*, 1027–1036. https://doi.org/10.1038/ncb3593.

19. Ullah, M.S., Davies, A.J., and Halestrap, A.P. (2006). The plasma membrane lactate transporter MCT4, but not MCT1, is up-regulated by hypoxia through a HIF-1alpha-dependent mechanism. J. Biol. Chem. *281*, 9030–9037. https://doi.org/10.1074/jbc.M511397200.

20. Meredith, D., and Christian, H.C. (2008). The SLC16 monocaboxylate transporter family. Xenobiotica *38*, 1072–1106. https://doi.org/10.1080/00498250802010868.

21. Hanahan, D., and Weinberg, R.A. (2011). Hallmarks of cancer: the next generation. Cell *144*, 646–674. https://doi.org/10.1016/j.cell.2011.02.013.

22. Dmitrieva-Posocco, O., Wong, A.C., Lundgren, P., Golos, A.M., Descamps, H.C., Dohnalová, L., Cramer, Z., Tian, Y., Yueh, B., Eskiocak, O., et al. (2022). Beta-hydroxybutyrate suppresses colorectal cancer. Nature *605*, 160–165. https://doi.org/10.1038/s41586-022-04649-6.

23. Zheng, X., Song, J., Yu, C., Zhou, Z., Liu, X., Yu, J., Xu, G., Yang, J., He, X., Bai, X., et al. (2022). Single-cell transcriptomic profiling unravels the adenoma-initiation role of protein tyrosine kinases during colorectal tumorigenesis. Signal Transduct. Target. Ther. *7*, 60. https://doi.org/10.1038/s41392-022-00881-8.

24. Pelka, K., Hofree, M., Chen, J.H., Sarkizova, S., Pirl, J.D., Jorgji, V., Bejnood, A., Dionne, D., Ge, W.H., Xu, K.H., et al. (2021). Spatially organized multicellular immune hubs in human colorectal cancer. Cell *184*, 4734–4752.e20. https://doi.org/10.1016/j.cell.2021.08.003.

25. Zhao, Z., Chen, X., Dowbaj, A.M., Sljukic, A., Bratlie, K., Lin, L., Fong, E.L.S., Balachander, G.M., Chen, Z., Soragni, A., et al. (2022). Organoids. Nat. Rev. Methods Primers *2*, 94. https://doi.org/10.1038/s43586-022-00174-y.

26. Bose, S., Clevers, H., and Shen, X. (2021). Promises and challenges of organoid-guided precision medicine. Med. *2*, 1011–1026. https://doi.org/10.1016/j.medj.2021.08.005.

27. Drost, J., van Jaarsveld, R.H., Ponsioen, B., Zimberlin, C., van Boxtel, R., Buijs, A., Sachs, N., Overmeer, R.M., Offerhaus, G.J., Begthel, H., et al. (2015). Sequential cancer mutations in cultured human intestinal stem cells. Nature *521*, 43–47. https://doi.org/10.1038/nature14415.

28. Oost, K.C., van Voorthuijsen, L., Fumagalli, A., Lindeboom, R.G.H., Sprangers, J., Omerzu, M., Rodriguez-Colman, M.J., Heinz, M.C., Verlaan-Klink, I., Maurice, M.M., et al. (2018). Specific labeling of stem cell activity in human colorectal organoids using an ASCL2-responsive minigene. Cell Rep. *22*, 1600–1614. https://doi.org/10.1016/j.celrep.2018.01.033.

29. Zhao, Y., Hu, Q., Cheng, F., Su, N., Wang, A., Zou, Y., Hu, H., Chen, X., Zhou, H.M., Huang, X., et al. (2015). SoNar, a highly responsive NAD⁺/NADH sensor, allows high-throughput metabolic screening of anti-tumor agents. Cell Metab. *21*, 777–789. https://doi.org/10.1016/j.cmet.2015.04.009.

30. Bermejo, C., Haerizadeh, F., Takanaga, H., Chermak, D., and Frommer, W.B. (2010). Dynamic analysis of cytosolic glucose and ATP levels in yeast using optical sensors. Biochem. J. *432*, 399–406. https://doi.org/10.1042/BJ20100946.

31. Takanaga, H., Chaudhuri, B., and Frommer, W.B. (2008). GLUT1 and GLUT9 as major contributors to glucose influx in HepG2 cells identified by a high sensitivity intramolecular FRET glucose sensor. Biochim. Biophys. Acta *1778*, 1091–1099. https://doi.org/10.1016/j.bbamem.2007.11.015.

32. San Martín, A., Ceballo, S., Ruminot, I., Lerchundi, R., Frommer, W.B., and Barros, L.F. (2013). A genetically encoded FRET lactate sensor and its use to detect the Warburg effect in single cancer cells. PLoS One *8*, e57712. https://doi.org/10.1371/journal.pone.0057712.

33. Williamson, D.H. (1967). The redox state of free Nicotimamide-Adenine Dinucleotide in the cytoplasm and mitochondria of rat liver. Biochem. J. *103*, 514–526.

34. Christensen, C.E., Karlsson, M., Winther, J.R., Jensen, P.R., and Lerche, M.H. (2014). Non-invasive in-cell determination of free cytosolic [NAD⁺]/[NADH] ratios using hyperpolarized glucose show large variations in metabolic phenotypes. J. Biol. Chem. *289*, 2344–2352. https://doi.org/10.1074/jbc.M113.498626.

35. Stringari, C., Wang, H., Geyfman, M., Crosignani, V., Kumar, V., Takahashi, J.S., Andersen, B., and Gratton, E. (2015). In vivo single-cell detection of metabolic oscillations in stem cells. Cell Rep. *10*, 1–7. https://doi.org/10.1016/j.celrep.2014.12.007.

36. Bonnay, F., Veloso, A., Steinmann, V., Köcher, T., Abdusselamoglu, M.D., Bajaj, S., Rivelles, E., Landskron, L., Esterbauer, H., Zinzen, R.P., et al. (2020). Oxidative metabolism drives immortalization of neural

CellPress
OPEN ACCESS

stem cells during tumorigenesis. Cell 182, 1490–1507.e19. https://doi.org/10.1016/j.cell.2020.07.039.

37. Xiao, W., Wang, R.S., Handy, D.E., and Loscalzo, J. (2018). NAD(H) and NADP(H) redox couples and cellular energy metabolism. Antioxid. Redox Signal. 28, 251–272. https://doi.org/10.1089/ars.2017.7216.

38. Ždralević, M., Brand, A., Di Ianni, L., Dettmer, K., Reinders, J., Singer, K., Peter, K., Schnell, A., Bruss, C., Decking, S.M., et al. (2018). Double genetic disruption of lactate dehydrogenases A and B is required to ablate the "Warburg effect" restricting tumor growth to oxidative metabolism. J. Biol. Chem. 293, 15947–15961. https://doi.org/10.1074/jbc.RA118.004180.

39. Claps, G., Faouzi, S., Quidville, V., Chehade, F., Shen, S., Vagner, S., and Robert, C. (2022). The multiple roles of LDH in cancer. Nat. Rev. Clin. Oncol. 19, 749–762. https://doi.org/10.1038/s41571-022-00686-2.

40. de la Cruz-López, K.G., Castro-Muñoz, L.J., Reyes-Hernández, D.O., García-Carrancá, A., and Manzo-Merino, J. (2019). Lactate in the regulation of tumor microenvironment and therapeutic approaches. Front. Oncol. 9, 1143. https://doi.org/10.3389/fonc.2019.01143.

41. Walenta, S., Chau, T.V., Schroeder, T., Lehr, H.A., Kunz-Schughart, L.A., Fuerst, A., and Mueller-Klieser, W. (2003). Metabolic classification of human rectal adenocarcinomas: a novel guideline for clinical oncologists? J. Cancer Res. Clin. Oncol. 129, 321–326. https://doi.org/10.1007/s00432-003-0450-x.

42. Hirayama, A., Kami, K., Sugimoto, M., Sugawara, M., Toki, N., Onozuka, H., Kinoshita, T., Saito, N., Ochiai, A., Tomita, M., et al. (2009). Quantitative metabolome profiling of colon and stomach cancer microenvironment by capillary electrophoresis time-of-flight mass spectrometry. Cancer Res. 69, 4918–4925. https://doi.org/10.1158/0008-5472.CAN-08-4806.

43. Schwitalla, S., Fingerle, A.A., Cammareri, P., Nebelsiek, T., Göktuna, S.I., Ziegler, P.K., Canli, O., Heijmans, J., Huels, D.J., Moreaux, G., et al. (2013). Intestinal tumorigenesis initiated by dedifferentiation and acquisition of stem-cell-like properties. Cell 152, 25–38. https://doi.org/10.1016/j.cell.2012.12.012.

44. Kok, R.N.U., Hebert, L., Huelsz-Prince, G., Goos, Y.J., Zheng, X., Bozek, K., Stephens, G.J., Tans, S.J., and van Zon, J.S. (2020). OrganoidTracker: efficient cell tracking using machine learning and manual error correction. PLoS One 15, e0240802. https://doi.org/10.1371/journal.pone.0240802.

45. Snippert, H.J., van der Flier, L.G., Sato, T., van Es, J.H., van den Born, M., Kroon-Veenboer, C., Barker, N., Klein, A.M., van Rheenen, J., Simons, B.D., et al. (2010). Intestinal crypt homeostasis results from neutral competition between symmetrically dividing Lgr5 stem cells. Cell 143, 134–144. https://doi.org/10.1016/j.cell.2010.09.016.

46. Lopez-Garcia, C., Klein, A.M., Simons, B.D., and Winton, D.J. (2010). Intestinal stem cell replacement follows a pattern of neutral drift. Science 330, 822–825. https://doi.org/10.1126/science.1196236.

47. Srinivasan, T., Walters, J., Bu, P., Than, E.B., Tung, K.L., Chen, K.Y., Panarelli, N., Milsom, J., Augenlicht, L., Lipkin, S.M., et al. (2016). NOTCH signaling regulates asymmetric cell fate of fast- and slow-cycling colon cancer-initiating cells. Cancer Res. 76, 3411–3421. https://doi.org/10.1158/0008-5472.CAN-15-3198.

48. Huelsz-Prince, G., Kok, R.N.U., Goos, Y., Bruens, L., Zheng, X., Ellenbroek, S., Van Rheenen, J., Tans, S., and van Zon, J.S. (2022). Mother cells control daughter cell proliferation in intestinal organoids to minimize proliferation fluctuations. eLife 11, e80682. https://doi.org/10.7554/eLife.80682.

49. Zheng, X., Betjes, M.A., Ender, P., Goos, Y.J., Huelsz-Prince, G., Clevers, H., van Zon, J.S., and Tans, S.J. (2023). Organoid cell fate dynamics in space and time. Sci. Adv. 9, 1–12. https://doi.org/10.1126/sciadv.add6480.

50. Moore, J.D., Staniszewska, A., Shaw, T., D'Alessandro, J., Davis, B., Surgenor, A., Baker, L., Matassova, N., Murray, J., Macias, A., et al. (2014). VER-246608, a novel pan-isoform ATP competitive inhibitor of pyruvate dehydrogenase kinase, disrupts Warburg metabolism and induces context-dependent cytostasis in cancer cells. Oncotarget 5, 12862–12876. https://doi.org/10.18632/oncotarget.2656.

51. Zhao, H., Yan, C., Hu, Y., Mu, L., Liu, S., Huang, K., Li, Q., Li, X., Tao, D., and Qin, J. (2020). Differentiated cancer cell-originated lactate promotes the self-renewal of cancer stem cells in patient-derived colorectal cancer organoids. Cancer Lett. 493, 236–244. https://doi.org/10.1016/j.canlet.2020.08.044.

52. Zowada, M.K., Tirier, S.M., Dieter, S.M., Krieger, T.G., Oberlack, A., Chua, R.L., Huerta, M., Ten, F.W., Laaber, K., Park, J., et al. (2021). Functional states in tumor-initiating cell differentiation in human colorectal cancer. Cancers (Basel) 13, 1097. https://doi.org/10.3390/cancers13051097.

53. Brooks, G.A., Curl, C.C., Leija, R.G., Osmond, A.D., Duong, J.J., and Arevalo, J.A. (2022). Tracing the lactate shuttle to the mitochondrial reticulum. Exp. Mol. Med. 54, 1332–1347. https://doi.org/10.1038/s12276-022-00802-3.

54. Lindeboom, R.G., van Voorthuijsen, L., Oost, K.C., Rodríguez-Colman, M.J., Luna-Velez, M.V., Furlan, C., Baraille, F., Jansen, P.W., Ribeiro, A., Burgering, B.M., et al. (2018). Integrative multi-omics analysis of intestinal organoid differentiation. Mol. Syst. Biol. 14, e8227. https://doi.org/10.15252/msb.20188227.

55. Beumer, J., and Clevers, H. (2021). Cell fate specification and differentiation in the adult mammalian intestine. Nat. Rev. Mol. Cell Biol. 22, 39–53. https://doi.org/10.1038/s41580-020-0278-0.

56. Fre, S., Huyghe, M., Mourikis, P., Robine, S., Louvard, D., and Artavanis-Tsakonas, S. (2005). Notch signals control the fate of immature progenitor cells in the intestine. Nature 435, 964–968. https://doi.org/10.1038/nature03589.

57. Dai, Z., Ramesh, V., and Locasale, J.W. (2020). The evolving metabolic landscape of chromatin biology and epigenetics. Nat. Rev. Genet. 21, 737–753. https://doi.org/10.1038/s41576-020-0270-8.

58. Chung, C.I., Sato, Y., Ohmuro-Matsuyama, Y., Machida, S., Kurumizaka, H., Kimura, H., and Ueda, H. (2019). Intrabody-based FRET probe to visualize endogenous histone acetylation. Sci. Rep. 9, 10188. https://doi.org/10.1038/s41598-019-46573-2.

59. Sansom, O.J., Meniel, V.S., Muncan, V., Phesse, T.J., Wilkins, J.A., Reed, K.R., Vass, J.K., Athineos, D., Clevers, H., and Clarke, A.R. (2007). Myc deletion rescues Apc deficiency in the small intestine. Nature 446, 676–679. https://doi.org/10.1038/nature05674.

60. He, T.C., Sparks, A.B., Rago, C., Hermeking, H., Zawel, L., da Costa, L.T., Morin, P.J., Vogelstein, B., and Kinzler, K.W. (1998). Identification of c-MYC as a target of the APC pathway. Science 281, 1509–1512. https://doi.org/10.1126/science.281.5382.1509.

61. Rennoll, S., and Yochum, G. (2015). Regulation of MYC gene expression by aberrant Wnt/beta-catenin signaling in colorectal cancer. World J. Biol. Chem. 6, 290–300. https://doi.org/10.4331/wjbc.v6.i4.290.

62. Röhrs, S., Kutzner, N., Vlad, A., Grunwald, T., Ziegler, S., and Müller, O. (2009). Chronological expression of Wnt target genes Ccnd1, Myc, Cdkn1a, Tfrc, Plf1 and Ramp3. Cell Biol. Int. 33, 501–508. https://doi.org/10.1016/j.cellbi.2009.01.016.

63. Munro, M.J., Peng, L., Wickremesekera, S.K., and Tan, S.T. (2020). Colon adenocarcinoma-derived cells that express induced-pluripotent stem cell markers possess stem cell function. PLoS One 15, e0232934. https://doi.org/10.1371/journal.pone.0232934.

64. Wan, M.L., Wang, Y., Zeng, Z., Deng, B., Zhu, B.S., Cao, T., Li, Y.K., Xiao, J., Han, Q., and Wu, Q. (2020). Colorectal cancer (CRC) as a multifactorial disease and its causal correlations with multiple signaling pathways. Biosci. Rep. 40, BSR20200265. https://doi.org/10.1042/BSR20200265.

65. Jorissen, R.N., Gibbs, P., Christie, M., Prakash, S., Lipton, L., Desai, J., Kerr, D., Aaltonen, L.A., Arango, D., Kruhøffer, M., et al. (2009). Metastasis-associated gene expression changes predict poor outcomes in patients with Dukes Stage B and C colorectal cancer. Clin. Cancer Res. 15, 7642–7651. https://doi.org/10.1158/1078-0432.CCR-09-1431.

66. de Sousa E Melo, F., Colak, S., Buikhuisen, J., Koster, J., Cameron, K., de Jong, J.H., Tuynman, J.B., Prasetyanti, P.R., Fessler, E., van den Bergh, S.P., et al. (2011). Methylation of cancer-stem-cell-associated Wnt target genes predicts poor prognosis in colorectal cancer patients. Cell Stem Cell 9, 476–485. https://doi.org/10.1016/j.stem.2011.10.008.

67. Liberzon, A., Birger, C., Thorvaldsdóttir, H., Ghandi, M., Mesirov, J.P., and Tamayo, P. (2015). The Molecular Signatures Database (MSigDB) hallmark gene set collection. Cell Syst. 1, 417–425. https://doi.org/10.1016/j.cels.2015.12.004.

68. Subramanian, A., Tamayo, P., Mootha, V.K., Mukherjee, S., Ebert, B.L., Gillette, M.A., Paulovich, A., Pomeroy, S.L., Golub, T.R., Lander, E.S., et al. (2005). Gene set enrichment analysis: A knowledge-basedapproach for interpreting genome-wideexpression profiles. Proc. Natl. Acad. Sci. USA 102, 15545–15550.

69. Hänzelmann, S., Castelo, R., and Guinney, J. (2013). GSVA: gene set variation analysis for microarray and RNA-Seq data. BMC Bioinformatics 14, 1–15.

70. Miller, D.M., Thomas, S.D., Islam, A., Muench, D., and Sedoris, K. (2012). c-Myc and cancer metabolism. Clin. Cancer Res. 18, 5546–5553. https://doi.org/10.1158/1078-0432.CCR-12-0977.

71. Dong, Y., Tu, R., Liu, H., and Qing, G. (2020). Regulation of cancer cell metabolism: oncogenic MYC in the driver's seat. Signal Transduct. Target. Ther. 5, 124. https://doi.org/10.1038/s41392-020-00235-2.

72. Trojer, P. (2022). Targeting BET bromodomains in cancer. Annu. Rev. Cancer Biol. 6, 313–336. https://doi.org/10.1146/annurev-cancerbio-070120-103531.

73. Lovén, J., Hoke, H.A., Lin, C.Y., Lau, A., Orlando, D.A., Vakoc, C.R., Bradner, J.E., Lee, T.I., and Young, R.A. (2013). Selective inhibition of tumor oncogenes by disruption of super-enhancers. Cell 153, 320–334. https://doi.org/10.1016/j.cell.2013.03.036.

74. Sun, H.Y., Du, S.T., Li, Y.Y., Deng, G.T., and Zeng, F.R. (2022). Bromodomain and extra-terminal inhibitors emerge as potential therapeutic avenues for gastrointestinal cancers. World J. Gastrointest. Oncol. 14, 75–89. https://doi.org/10.4251/wjgo.v14.i1.75.

75. Huang, M.J., Cheng, Y.C., Liu, C.R., Lin, S., and Liu, H.E. (2006). A small-molecule c-Myc inhibitor, 10058-F4, induces cell-cycle arrest, apoptosis, and myeloid differentiation of human acute myeloid leukemia. Exp. Hematol. 34, 1480–1489. https://doi.org/10.1016/j.exphem.2006.06.019.

76. Morris, L.G.T., Riaz, N., Desrichard, A., Şenbabaoğlu, Y., Hakimi, A.A., Makarov, V., Reis-Filho, J.S., and Chan, T.A. (2016). Pan-cancer analysis of intratumor heterogeneity as a prognostic determinant of survival. Oncotarget 7, 10051–10063.

77. Jamal-Hanjani, M., Wilson, G.A., McGranahan, N., Birkbak, N.J., Watkins, T.B.K., Veeriah, S., Shafi, S., Johnson, D.H., Mitter, R., Rosenthal, R., et al. (2017). Tracking the evolution of non-small-cell lung cancer. N. Engl. J. Med. 376, 2109–2121. https://doi.org/10.1056/NEJMoa1616288.

78. Li, S., Garrett-Bakelman, F.E., Chung, S.S., Sanders, M.A., Hricik, T., Rapaport, F., Patel, J., Dillon, R., Vijay, P., Brown, A.L., et al. (2016). Distinct evolution and dynamics of epigenetic and genetic heterogeneity in acute myeloid leukemia. Nat. Med. 22, 792–799. https://doi.org/10.1038/nm.4125.

79. Janiszewska, M., Tabassum, D.P., Castaño, Z., Cristea, S., Yamamoto, K.N., Kingston, N.L., Murphy, K.C., Shu, S., Harper, N.W., Del Alcazar, C.G., et al. (2019). Subclonal cooperation drives metastasis by modulating local and systemic immune microenvironments. Nat. Cell Biol. 21, 879–888. https://doi.org/10.1038/s41556-019-0346-x.

80. Marusyk, A., Tabassum, D.P., Altrock, P.M., Almendro, V., Michor, F., and Polyak, K. (2014). Non-cell-autonomous driving of tumour growth supports sub-clonal heterogeneity. Nature 514, 54–58. https://doi.org/10.1038/nature13556.

81. Calbo, J., van Montfort, E., Proost, N., van Drunen, E., Beverloo, H.B., Meuwissen, R., and Berns, A. (2011). A functional role for tumor cell heterogeneity in a mouse model of small cell lung cancer. Cancer Cell 19, 244–256. https://doi.org/10.1016/j.ccr.2010.12.021.

82. Lee, D.C., Sohn, H.A., Park, Z.Y., Oh, S., Kang, Y.K., Lee, K.M., Kang, M., Jang, Y.J., Yang, S.J., Hong, Y.K., et al. (2015). A lactate-induced response to hypoxia. Cell 161, 595–609. https://doi.org/10.1016/j.cell.2015.03.011.

83. Liu, S., Zhao, H., Hu, Y., Yan, C., Mi, Y., Li, X., Tao, D., and Qin, J. (2022). Lactate promotes metastasis of normoxic colorectal cancer stem cells through PGC-1alpha-mediated oxidative phosphorylation. Cell Death Dis. 13, 651. https://doi.org/10.1038/s41419-022-05111-1.

84. Wei, Y., Xu, H., Dai, J., Peng, J., Wang, W., Xia, L., and Zhou, F. (2018). Prognostic significance of serum lactic acid, lactate dehydrogenase, and albumin levels in patients with metastatic colorectal cancer. BioMed Res. Int. 2018, 1804086. https://doi.org/10.1155/2018/1804086.

85. Wang, Z.H., Peng, W.B., Zhang, P., Yang, X.P., and Zhou, Q. (2021). Lactate in the tumour microenvironment: from immune modulation to therapy. EBiomedicine 73, 103627. https://doi.org/10.1016/j.ebiom.2021.103627.

86. Sun, Q., Wu, J., Zhu, G., Li, T., Zhu, X., Ni, B., Xu, B., Ma, X., and Li, J. (2022). Lactate-related metabolic reprogramming and immune regulation in colorectal cancer. Front. Endocrinol. (Lausanne) 13, 1089918. https://doi.org/10.3389/fendo.2022.1089918.

87. Halestrap, A.P. (2013). The SLC16 gene family - structure, role and regulation in health and disease. Mol. Aspects Med. 34, 337–349. https://doi.org/10.1016/j.mam.2012.05.003.

88. Halestrap, A.P. (2012). The monocarboxylate transporter family–Structure and functional characterization. IUBMB Life 64, 1–9. https://doi.org/10.1002/iub.573.

89. Srivastava, S., Gajwani, P., Jousma, J., Miyamoto, H., Kwon, Y., Jana, A., Toth, P.T., Yan, G., Ong, S.G., and Rehman, J. (2023). Nuclear translocation of mitochondrial dehydrogenases as an adaptive cardioprotective mechanism. Nat. Commun. 14, 4360. https://doi.org/10.1038/s41467-023-40084-5.

90. Hu, Y., Zhou, J., Ye, F., Xiong, H., Peng, L., Zheng, Z., Xu, F., Cui, M., Wei, C., Wang, X., et al. (2015). BRD4 inhibitor inhibits colorectal cancer growth and metastasis. Int. J. Mol. Sci. 16, 1928–1948. https://doi.org/10.3390/ijms16011928.

91. Zhang, Y., Tian, S., Xiong, J., Zhou, Y., Song, H., and Liu, C. (2018). JQ-1 inhibits colon cancer proliferation via suppressing Wnt/beta-catenin signaling and miR-21. Chem. Res. Toxicol. 31, 302–307. https://doi.org/10.1021/acs.chemrestox.7b00346.

92. Certo, M., Llibre, A., Lee, W., and Mauro, C. (2022). Understanding lactate sensing and signalling. Trends Endocrinol. Metab. 33, 722–735. https://doi.org/10.1016/j.tem.2022.07.004.

93. Jin, L., Guo, Y., Chen, J., Wen, Z., Jiang, Y., and Qian, J. (2022). Lactate receptor HCAR1 regulates cell growth, metastasis and maintenance of cancer-specific energy metabolism in breast cancer cells. Mol. Med. Rep. 26, 268. https://doi.org/10.3892/mmr.2022.12784.

94. Zhang, D., Tang, Z., Huang, H., Zhou, G., Cui, C., Weng, Y., Liu, W., Kim, S., Lee, S., Perez-Neut, M., et al. (2019). Metabolic regulation of gene expression by histone lactylation. Nature 574, 575–580. https://doi.org/10.1038/s41586-019-1678-1.

95. Freeman, T.J., Smith, J.J., Chen, X., Washington, M.K., Roland, J.T., Means, A.L., Eschrich, S.A., Yeatman, T.J., Deane, N.G., and Beauchamp, R.D. (2012). Smad4-mediated signaling inhibits intestinal neoplasia by inhibiting expression of beta-catenin. Gastroenterology 142, 562–571.e2. https://doi.org/10.1053/j.gastro.2011.11.026.

96. Tian, X., Du, H., Fu, X., Li, K., Li, A., and Zhang, Y. (2009). Smad4 restoration leads to a suppression of Wnt/beta-catenin signaling activity and migration capacity in human colon carcinoma cells. Biochem. Biophys. Res. Commun. 380, 478–483. https://doi.org/10.1016/j.bbrc.2009.01.124.

97. Perekatt, A.O., Shah, P.P., Cheung, S., Jariwala, N., Wu, A., Gandhi, V., Kumar, N., Feng, Q., Patel, N., Chen, L., et al. (2018). SMAD4 suppresses

WNT-driven dedifferentiation and oncogenesis in the differentiated gut epithelium. Cancer Res. *78*, 4878–4890. https://doi.org/10.1158/0008-5472.CAN-18-0043.

98. Bolden, J.E., Tasdemir, N., Dow, L.E., van Es, J.H., Wilkinson, J.E., Zhao, Z., Clevers, H., and Lowe, S.W. (2014). Inducible in vivo silencing of Brd4 identifies potential toxicities of sustained BET protein inhibition. Cell Rep. *8*, 1919–1929. https://doi.org/10.1016/j.celrep.2014.08.025.

99. Ludikhuize, M.C., Gevers, S., Nguyen, N.T.B., Meerlo, M., Roudbari, S.K.S., Gulersonmez, M.C., Stigter, E.C.A., Drost, J., Clevers, H., Burgering, B.M.T., et al. (2022). Rewiring glucose metabolism improves 5-FU efficacy in p53-deficient/KRAS(G12D) glycolytic colorectal tumors. Commun. Biol. *5*, 1159. https://doi.org/10.1038/s42003-022-04055-8.

100. Warren, L., Manos, P.D., Ahfeldt, T., Loh, Y.H., Li, H., Lau, F., Ebina, W., Mandal, P.K., Smith, Z.D., Meissner, A., et al. (2010). Highly efficient re-programming to pluripotency and directed differentiation of human cells with synthetic modified mRNA. Cell Stem Cell *7*, 618–630. https://doi.org/10.1016/j.stem.2010.08.012.

101. Wiederschain, D., Wee, S., Chen, L., Loo, A., Yang, G., Huang, A., Chen, Y., Caponigro, G., Yao, Y.M., Lengauer, C., et al. (2009). Single-vector inducible lentiviral RNAi system for oncology target validation. Cell Cycle *8*, 498–504. https://doi.org/10.4161/cc.8.3.7701.

102. R Team (2023). R: A Language and Environment for Statistical Computing (R Foundation for Statistical Computing).

103. Posit Team (2022). RStudio: Integrated Development Environment for R. Posit Software (PBC), MA2024.

104. Schmidt, U., Weigert, M., Broaddus, C., and Myers, G. (2018). Cell Detection with Star-Convex Polygons. In Medical Image Computing and Computer Assisted Intervention – MICCAI 2018. Lecture Notes in Computer Science. pp. 265–273.

105. Van Lidth de Jeude, J.F., Vermeulen, J.L.M., Montenegro-Miranda, P.S., Van den Brink, G.R., and Heijmans, J. (2015). A protocol for lentiviral transduction and downstream analysis of intestinal organoids. J. Vis. Exp. 52531. https://doi.org/10.3791/52531.

106. Ahrens, J., Geveci, Berk, and Law, C. (2005). An End-User Tool for Large Data Visualization, Visualization Handbook (Elsevier).

107. Ludikhuize, M.C., Meerlo, M., Burgering, B.M.T., and Rodríguez Colman, M.J. (2021). Protocol to profile the bioenergetics of organoids using sea-horse. Star Protoc. *2*, 100386. https://doi.org/10.1016/j.xpro.2021.100386.

108. Zeller, P., Yeung, J., Viñas Gaza, H., de Barbanson, B.A., Bhardwaj, V., Florescu, M., van der Linden, R., and van Oudenaarden, A. (2023). Single-cell sortChIC identifies hierarchical chromatin dynamics during hematopoiesis. Nat. Genet. *55*, 333–345. https://doi.org/10.1038/s41588-022-01260-3.

109. Artegiani, B., van Voorthuijsen, L., Lindeboom, R.G.H., Seinstra, D., Heo, I., Tapia, P., López-Iglesias, C., Postrach, D., Dayton, T., Oka, R., et al. (2019). Probing the tumor suppressor function of BAP1 in CRISPR-engi-neered human liver organoids. Cell Stem Cell *24*, 927–943.e6. https://doi.org/10.1016/j.stem.2019.04.017.

110. Sauvola, J., and Pietikäinen, M. (2000). Adaptive document image binar-ization. Pattern Recognit. *33*, 225–236.

111. Hao, Y., Hao, S., Andersen-Nissen, E., Mauck, W.M., 3rd, Zheng, S., Butler, A., Lee, M.J., Wilk, A.J., Darby, C., Zager, M., et al. (2021). Integrated analysis of multimodal single-cell data. Cell *184*, 3573–3587.e29. https://doi.org/10.1016/j.cell.2021.04.048.

112. Ianevski, A., Giri, A.K., and Aittokallio, T. (2022). Fully-automated and ul-tra-fast cell-type identification using specific marker combinations from single-cell transcriptomic data. Nat. Commun. *13*, 1246. https://doi.org/10.1038/s41467-022-28803-w.

113. Gautier, L., Cope, L., Bolstad, B.M., and Irizarry, R.A. (2004). affy–anal-ysis of Affymetrix GeneChip data at the probe level. Bioinformatics *20*, 307–315.

114. Huber, W., Carey, V.J., Gentleman, R., Anders, S., Carlson, M., Carvalho, B.S., Bravo, H.C., Davis, S., Gatto, L., Girke, T., et al. (2015).

Orchestrating high-throughput genomic analysis with Bioconductor. Nat. Methods *12*, 115–121.

115. Durinck, S., Spellman, P.T., Birney, E., and Huber, W. (2009). Mapping identifiers for the integration of genomic datasets with the R/Bioconductor package biomaRt. Nat. Protoc. *4*, 1184–1191. https://doi.org/10.1038/nprot.2009.97.

116. Li, H. (2013). Aligning sequence reads,clone sequences and assembly contigs with BWA-MEM. Preprint at arXiv. https://doi.org/10.48550/arXiv.1303.3997.

117. de Barbanson, B., Marloes, Bhardwaj, V., Yeung, J., J-PTRson, and Alemany, A. (2023). BuysDB/SingleCellMultiOmics: 0.1.32. Zenodo. https://doi.org/10.5281/zenodo.7826155.

118. Amemiya, H.M., Kundaje, A., and Boyle, A.P. (2019). The ENCODE black-list: identification of problematic regions of the genome. Sci. Rep. *9*, 9354. https://doi.org/10.1038/s41598-019-45839-z.

119. Maarten van der Sande, S.F., Smits, J., Schäfers, T., Snabel, R., and van Heeringen, S. (2024). seq2science. Zenodo. https://doi.org/10.5281/zenodo.10619482.

120. Liao, Y., Smyth, G.K., and Shi, W. (2019). The R package Rsubread is easier, faster, cheaper and better for alignment and quantification of RNA sequencing reads. Nucleic Acids Res. *47*, e47. https://doi.org/10.1093/nar/gkz114.

121. Love, M.I., Huber, W., and Anders, S. (2014). Moderated estimation of fold change and dispersion for RNA-seq data with DESeq2. Genome Biol. *15*, 550. https://doi.org/10.1186/s13059-014-0550-8.

122. Gu, Z., Eils, R., and Schlesner, M. (2016). Complex heatmaps reveal pat-terns and correlations in multidimensional genomic data. Bioinformatics *32*, 2847–2849.

123. Liis Kolberg, U.R., Kuzmin, I., Vilo, J., and Peterson, H. (2020). gprofiler2-an R Package for Gene List Functional Enrichment Analysis and Namespace Conversion Toolset g:Profiler. F1000Research *9*, ELIXIR-709.

124. Putri, G.H., Anders, S., Pyl, P.T., Pimanda, J.E., and Zanini, F. (2022). Analysing high-throughput sequencing data in Python with HTSeq 2.0. Bioinformatics *38*, 2943–2945. https://doi.org/10.1093/bioinformatics/btac166.

125. Broad Institute (2019). Picard toolkit. https://broadinstitute.github.io/picard/.

126. Anders, S., Pyl, P.T., and Huber, W. (2015). HTSeq–a Python framework to work with high-throughput sequencing data. Bioinformatics *31*, 166–169.

127. Andrews, S. (2010). FastQC: A quality control tool for high throughput sequence data. http://www.bioinformatics.babraham.ac.uk/projects/fastqc/.

128. Krueger, F. (2021). Trim Galore. https://github.com/FelixKrueger/TrimGalore/tree/0.6.7.

129. Kopylova, E., Noé, L., and Touzet, H. (2012). SortMeRNA: fast and accu-rate filtering of ribosomal RNAs in metatranscriptomic data. Bioinformatics *28*, 3211–3217. https://doi.org/10.1093/bioinformatics/bts611.

130. Dobin, A. (2024). STAR: Spliced Transcripts Alignment to a Reference. https://github.com/alexdobin/STAR/.

131. Tarasov, A., Vilella, A.J., Cuppen, E., Nijman, I.J., and Prins, P. (2015). Sambamba: fast processing of NGS alignment formats. Bioinformatics *31*, 2032–2034. https://doi.org/10.1093/bioinformatics/btv098.

132. Wang, L., Wang, S., and Li, W. (2012). RSeQC: quality control of RNA-seq experiments. Bioinformatics *28*, 2184–2185. https://doi.org/10.1093/bioinformatics/bts356.

133. Smith, Lab. (2022). PreSeq. https://github.com/smithlabcode/preseq.

134. Liao, Y., Smyth, G.K., and Shi, W. (2014). featureCounts: an efficient gen-eral-purpose program for assigning sequence reads to genomic fea-tures. Bioinformatics *30*, 923–930. https://doi.org/10.1093/bioinformat-ics/btt656.

STAR★METHODS

KEY RESOURCES TABLE

REAGENT or RESOURCE	SOURCE	IDENTIFIER
Antibodies		
KRT20	Dako	Cat#M7019; RRID:AB_2133718
KI67	Abcam	Cat#ab15580; RRID:AB_443209
MCT4	Santa Cruz	Cat#sc-50329 (H-90); RRID:AB_2189333
MCT4	Santa Cruz	Cat#sc-376140 (D-1); RRID:AB_10992036
MCT1	Santa Cruz	Cat#sc-365501 (H-1); RRID:AB_10841766
HIF1α	Cell Signaling	Cat#36169 (D1S7W); RRID:AB_2799095
CAIX	Novus Biologicals	Cat##NB100-417SS; RRID:AB_788423
H3K27ac	Abcam	Cat#ab4729; RRID:AB_2118291
MYC	Santa Cruz	Cat#sc-40 (9E10); RRID:AB_627268
MYC	Abcam	Cat#ab32072 (Y69); RRID:AB_731658
β-catenin	BD Transduction Laboratories™	Cat#610154; RRID:AB_397555
Goat Anti-Rabbit IgG (H+L)-HRP Conjugate	Biorad	Cat#170-6515; RRID:AB_11125142
Goat Anti- Mouse IgG (H+L)-HRP Conjugate	Biorad	Cat#170-6516; RRID:AB_11125547
Goat anti-Mouse IgG (H+L), Alexa Fluor™ 488	Invitrogen	Cat#A-11029; RRID:AB_2534088
Goat anti-Rabbit IgG (H+L), Alexa Fluor™ 488	Invitrogen	Cat#A-11034; RRID:AB_2576217
Goat anti-Mouse IgG (H+L), Alexa Fluor™ 568	Invitrogen	Cat#A-11031; RRID:AB_144696
Goat anti- Rabbit IgG (H+L), Alexa Fluor™ 568	Invitrogen	Cat#A-11036; RRID:AB_10563566
Goat anti-Mouse IgG (H+L), Alexa Fluor™ 647	Invitrogen	Cat#A-21236; RRID:AB_2535805
Goat anti- Rabbit IgG (H+L), Alexa Fluor™ 647	Invitrogen	Cat#A-21245; RRID:AB_2535813
Hoechst 33342	Life Technologies	Cat#H1399
H3Kpanac (acetyl K9 + K14 + K18 + K23 + K27)	Abcam	Cat#ab47915; RRID:AB_873860
DAPI	Sigma-Aldrich	Cat#D9564
H3K9ac	EpiCypher	Cat#13-0033
H3	Abcam	Cat#ab1791; RRID:AB_302613
PDHA1	Invitrogen	Cat#459400; RRID:AB_10375326
pPDHA1 (S293)	Abcam	Cat#ab92696; RRID:AB_10711672
Vinculin	Sigma-Aldrich	Cat#V9131; RRID:AB_477629
GAPDH	Merck Millipore	Cat#MAB374; RRID:AB_2107445
Mitotracker Deep red	Thermofisher	Cat#M22426
MitoTracker Green	Thermofisher	Cat#M7514
Chemicals, peptides, and recombinant proteins		
DMEM F12	Gibco	Cat#12634-010
SILAC Advanced DMEM/F-12 Flex Media	Gibco	Cat#A24943-01
DMEM – low glucose (HEK293T cells)	Sigma-Aldrich	Cat#D5546
B27	Fisher Scientific	Cat#15360284
R-spondin-CM	in-house	N/A
Noggin-CM	in-house	N/A
Nicotinamide (Nico)	Sigma-Aldrich	Cat#A9165
Wnt surrogate FC fusion protein	U-protein express BV	Cat#N001
EGF	Peprotech	Cat#AF-100-15
Fetal Bovine Serum (FBS)	BODINCO BV	Cat#S00KL10004
Y-27632	Gentaur	Cat#607-A3008
A83	Biotechne	Cat#2939
SB202190 (SB)	Gentaur	Cat#607-A1632

(Continued on next page)

Continued

REAGENT or RESOURCE	SOURCE	IDENTIFIER
HEPES	Gibco	15630-056
N-acetyl-cysteine (NAC)	Sigma-Aldrich	Cat#N0636
Glutamine	Lonza	Cat#17-605E
GlutaMAX (Glutamine)	Gibco	Cat#35050-038
L-Arginine	Sigma-Aldrich	Cat#A6969
L-Lysine	Sigma-Aldrich	Cat#L8662
D-Glucose	Merck Millipore	Cat#1.08337.1000
Sodium L-Lactate	Sigma-Aldrich	Cat#71718
Sodium Pyruvate	Sigma-Aldrich	Cat#P5280/S8636
BME	Bio-Techne	Cat#3533-010-02
Matrigel	Corning	Cat#356231
Puromycin	InvivoGen	ant-pr-1
Blasticidin	InvivoGen	ant-bl
Geneticin (G418)	Thermofisher	Cat#11811064
Penicillin/ Streptomycin	Sigma-Aldrich	Cat#P0781
DCA	Sigma-Aldrich	Cat#347795
Oligomycin	Sigma-Aldrich	Cat#75351
Rotenone	Sigma-Aldrich	Cat#R8875
Antimycin-A	Sigma-Aldrich	Cat#A8674
FCCP	Sigma-Aldrich	Cat#C2920
BPTES	Sigma-Aldrich	Cat#SML0601
Etomoxir	Merck Life science	Cat#E1905
UK5099	Merck Life science	Cat#PZ0160
JQ1	Abcam	Cat#1268524-70-4
IBET762	Medchemexpress	Cat#1260907-17-2
A485	Biotechne/Tocris	Cat#1889279-16-6
GSK2837808A	Medchem express	Cat#HY-100681
VER-246608	MedChemExpress	Cat#HY-12492
VB124	MedChemExpress	Cat#HY-139665
AZD3965	MedChemExpress	Cat#HY-12750
10058-F4	MedChemExpress	Cat#403811-55-2
Syrosingopine	Sigma-Aldrich	Cat#84-36-6
Deposited data		
scRNAseq datasets	Dmitrieva-Posocco et al.,[22] Pelka et al.,[24] and Zheng et al.[23]	GEO: GSE196964, GEO: GSE178341, GEO: GSE161277
Microarray	Jorissen et al.[65] and de Sousa et al.[66]	GEO: GSE14333 (290 patients), GEO: GSE33113 (96 patients)
Data S1: Source data underlying all plots and figures	This paper	N/A
Metabolomics data	This paper	MetaboLights: MTBLS11849
ATACseq, RNAseg and bulkChICseq data	This paper	E GA: EGAS50000000063
Experimental models: Cell lines		
Human: Colon wild type (WT) and TPOs (TPO3/4) organoids[27]	Hans Clevers and Jarno Drost laboratory	N/A
Human: WT/TPO3/4 STAR-dTomato-NLS organoids	Ludikhuize et al.[99]	N/A
Human: TPO3/4 STAR-dTomato-NLS H2B-SoNar	This paper	N/A
Human: TPO3 STAR-dTomato-NLS indGFP-MYC	This paper	N/A
Human: TPO3 STAR-dTomato-NLS indMYC	This paper	N/A
Human: TPO3 STAR-mcherry-NLS	This paper	N/A

Continued

REAGENT or RESOURCE	SOURCE	IDENTIFIER
Human: TPO3 STAR-dTomato-NLS H2B-SoNar shMYC	This paper	N/A
Human: TPO3/4 STAR- dTomato-NLS smH3K9ac H1-maroon	This paper	N/A
Human: TPO3 STAR- dTomato-NLS Laconic-NLS	This paper	N/A
Human: TPO3 STAR- dTomato-NLS FLII12Pglu-700uDelta6	Ludikhuize et al.[99]	N/A
Biological samples		
Paraffin-embedded tissue from healthy and tumour colon tissues of human origin	UMC Utrecht biobank committee	protocol #18-222
Oligonucleotides		
shRNA targeting sequence MYC: CCTGAGACAGATCAGCAACAA	Sigma-Aldrich	TRCN0000039642
Primers for qPCR, see Table S4	This paper	N/A
Recombinant DNA		
8xSTAR-dTomato-NLS-puro	Ludikhuize et al.[99]	N/A
pInducer-CW-SoNar	Zhao et al.[29]	N/A
phEF1-H2B-SoNar-blast	This paper	N/A
laconic/pcDNA3.1	Addgene, San Martin et al.[32]	Cat#44238
phEF1-Laconic-NLS-blast	This paper	N/A
phEF1-smH3K9ac-blast	This paper, Chung et al.[58]	N/A
pLenti-H1-maroon	H. Snippert laboratory	N/A
phEF1-FLII12Pglu-700uDelta6-puro	Ludikhuize et al.[99]	N/A
pLenti-Tet-ON-GFP-MYC-neo	This paper, Warren et al.[100]	N/A
pLenti-Tet-ON-MYC-blast	This paper, Warren et al.[100]	N/A
Tet-pLKO-puro	Addgene, Wiederschain et al.[101]	Cat#21915
Tet-pLKO-shMYC-blast	This paper	N/A
Software and algorithms		
CellPhenTracker	This paper	https://github.com/RodriguezColmanLab/CellPhenTracker.git
OrganoidTracker	Kok et al.[44]	https://github.com/jvzonlab/OrganoidTracker.git
R 4.2.3[102]	R Foundation for Statistical Computing	https://www.R-project.org/
RStudio 2024.9.1.394	RStudio Team[103]	http://www.posit.co/
Python 3.10	Python Software Foundation	https://www.python.org/psf-landing/
GraphPad Prism 10	Adobe	https://www.graphpad.com/scientific-software/prism/
Fiji	ImageJ	https://imagej.net/Fiji
Stardist ImageJ plugin	Schmidt et al.[104]	https://github.com/stardist/stardist-imagej.git
Quan Browser Thermo Xcalibur 4.7.69.37	Thermo Fisher Scientific	N/A
Adobe Illustrator	N/A	https://www.adobe.com/nl/products/ illustrator.html
Critical commercial assays		
More information can be found in Table S3	This paper	N/A
Other		
Other reagents used in this paper, see Table S3	This paper	N/A

EXPERIMENTAL MODEL AND STUDY PARTICIPANT DETAILS

Wild type and tumour progression organoids (TPO3 and TPO4)[27] were a gift from the Hans Clevers lab and the Jarno Drost lab. Organoid line information has been previously reported.[27] For passaging, organoids were tryped into single cells or small clumps of cells and plated in Matrigel or BME in DMEM F12 expansion medium (see Table S1), supplemented with 1% penicillin/ streptomycin, 10 mM HEPES, 2 mM Glutamine and ROCK inhibitor Y-27632 (1:1000). The organoids were kept at 37 °C and at 5% CO_2. The culture medium was replaced every 2 to 3 days.

For experiment setup, five to seven days post-trypsinization, the organoids were reseeded in fresh BME or Matrigel, and the culture medium was switched to SILAC differentiation medium (see Table S1). This medium was prepared by supplementing SILAC Advanced DMEM/F12 Flex Medium with 1% penicillin/ streptomycin, 10 mM HEPES, 2 mM Glutamine, L-Arginine (147.5 mg/L) and L-Lysine (91.25 mg/L). The control medium was prepared by supplementing SILAC differentiation medium with 12 mM of D-glucose. The lactate and pyruvate medium were prepared by respectively adding 23 mM of sodium L-lactate or sodium pyruvate, in addition to 0.5 mM glucose, to SILAC differentiation medium. Glucose-gradient media were prepared by supplementing SILAC differentiation medium with different D-glucose concentrations (18, 10 and 0.5 mM).

METHOD DETAILS

Cloning

The 8xSTAR-dTomato-NLS-puro (STAR-dTomato-NLS) was reconstructed from STAR plasmid developed by Oost et al.[28] The STAR-mCherry-NLS construct was generated by replacing the dTomato sequence with the mCherry sequence. The pInducer-CW-SoNar plasmid was a gift from Zhao et al. (Shanghai, China).[29] The H2B-SoNar sequence was cloned into a constitutive expressing plenty backbone with a hEF1 promoter and a blasticidin resistance cassette (phEF1-H2B-SoNar-blast). From laconic/ pcDNA3.1[32] (addgene #44238), mTFP1-Lac-mVenus sequence was PCR out with an introduced NLS at the mVenus tail. The sequence was then inserted into plenti backbone with a hEF1 promoter and a blasticidin resistance cassette, generating Laconic-NLS reporter. The smH3K9ac FRET sensor was cloned by replacing SoNar sequence from phEF1-H2B-SoNar-blast with the Ypet-scFv-sECFP (H3K9ac) sequence obtained as a gift from Chung et al. (Kanagawa, Japan).[58] The sECFP sequence was replaced with a codon-silent-mutated ECFP (smECFP) sequence to avoid high incidence of recombination with Ypet. H1-maroon plasmid was a gift from Snipper group (Utrecht, Netherlands). The FLII12Pglu-700uDelta6[31] (addgene #17866) was optimized for lentiviral infection as explained previously.[99] The inducible MYC (indMYC) was constructed by introducing *MYC* sequence[100] (addgene #26818) into a Tet-ON plasmid system with a neomycin resistance cassette. For visualizing MYC, the GFP sequence was fused to N-terminal of *MYC* using a SGLRSTSAA linker, including a blasticidin resistance cassette (indGFP-MYC). To knock down MYC, an inducible knockdown system was constructed using the Tet-pLKO[101] (addgene #21915) vector, incorporating a target sequence (5'-CCTGAGACAGATCAGCAACAA-3' #Sigma-Aldrich- TRCN0000039642) specific to *MYC*. For stable selection, a blasticidin resistance cassette was included in the vector.

Lentiviral transduction

The interested constructs, together with a third-generation packaging vectors and LentiX Concentrator (1x), were used to generate and concentrate lentiviral particles. HEK293T cells were grown in DMEM low glucose medium supplemented with 10% FBS, 1% penicillin/ streptomycin and 2 mM Glutamine and were used for the production of lentiviral particles. TPO3/4 STAR-dTomato-NLS H2B-SoNar, TPO3/4 STAR-dTomato-NLS Laconic-NLS, TPO3/4 STAR-dTomato-NLS smH3K9ac H1-maroon, TPO3/4 STAR-dTomato-NLS Glu700, TPO3/4 ind(GFP-)MYC STAR-NLS organoid lines were generated through lentiviral transduction as described previously.[105] Next, the infected organoids were selected with puromycin 3.33 μg/mL or blasticidin 13.33-20 μg/mL or with geneticin 400 μg/mL. When necessary, FACS was performed to enrich the population of cells positively expressing the target markers.

FACS sorting

For transcription and protein analysis between different cancer cell types, TPO3/4 STAR-dTomato-NLS were trypsinized into single cells in suspension (DMEM supplemented with ROCK inhibitor Y-27632 1:1000). DAPI was added to exclude dead cells. FACS sorting was performed with FACS ARIA II/III with a gating strategy based on the top and bottom 17% of the STAR-dTomato-NLS signal.

Immunofluorescent (IF) staining in organoids

Organoids were collected in 1:1 mix of ice-cold cell recovery solution and of ice-cold phosphate-buffered saline (PBS). Organoids were incubated on ice for 10 minutes and were washed again with ice-cold PBS. Next, they were fixed by 4% paraformaldehyde for 30 minutes at room temperature (RT) and stored in PBS at 4 °C for up to 4 days. For staining, organoids were transferred into 1.5 mL eppendorfs and were permeabilized/blocked with PBS buffer containing 10% DMSO, 2% Triton X-100, and 10 g/L bovine serum albumin (BSA) for 2 hours at 4 °C. Organoids were stained overnight with primary antibodies (KRT20 1:200, KI67 1:200, H3K27ac 1:200, MCT4 1:200, HIF1α 1:1000), followed by Alexa fluorophore-conjugated secondary antibodies (+DAPI) for 4 hours at 4 °C. Imaging was performed using a SP8 confocal microscope (Leica Microsystems).

Immunohistochemistry (IHC) staining
Fluorescent detection
Slides of paraffin-embedded tissue of healthy and tumour colon tissues included according to the no-objection-agreement, approved by the UMC Utrecht biobank committee (protocol #18–222). In brief, slides were baked at 60 °C for 2 hours and were dewaxed in xylene and rehydrated in graded alcohol baths. The slides were incubated in preheated antigen retrieval solution, either citrate pH6 (2.94 g/L tri-sodium citrate in MQ) or TE pH 9.5 (Tris 10 mM EDTA 1 mM pH 9.5)) at 96 °C for 30 minutes. Nonspecific binding sites were blocked in Tris-buffered saline (TBS) containing 2-3% BSA and Fc receptor blockers 1:100 for 60 minutes at RT. Primary antibodies (KRT20 1:100, KI67 1:100, H3K27ac 1:200, MCT4 H-90 1:200, MCT1 1:100, CAIX 1:500) were diluted in TBS 0.5% BSA overnight at 4 °C, followed by incubation with Alexa-fluorophore-conjugated secondary antibodies and DAPI for 1 hour at RT. Imaging was performed using an Imager Z1 non-confocal or LSM880 confocal microscope (Zeiss Microsystems).
Chromogenic detection
Dewaxing and antigen retrieval steps were identical to *Fluorescent detection*, except that slides were incubated with 3.33% H_2O_2 in PBS for 15 minutes and washed in TBS to quench endogenous peroxydase activity before antigen retrieval step. Slides were blocked for 30 minutes followed by primary antibody application (MYC 1:50, β-catenin 1:200). Then the slides were washed with TBS and incubated with Goat-anti-rabbit HRP in blocking solution before another washing with PBS. Before mounting, signals were developed with DAB kit, followed by a 1–2 minute hematoxylin counterstain. Imaging was performed by Pathology department (Hamamatsu Nano Zoomer).

Mitochondrial live imaging
Organoids were incubated with MitoTracker Deep red (200 nM) and Hoechst (10 μg/mL) for 30 minutes at 37 °C and washed. Stained organoids were imaged with SP8 confocal microscope (Leica Microsystems).

Live imaging of organoids
Organoids were cultured in differentiation medium (see Table S1) for one or two days before the start of the time-lapse experiments. To examining the effects of different treatments on cell fate during organoid development, the treatment (lactate, DCA, doxycycline, JQ1 or 10058-F4) were added just prior to imaging. Imaging was performed using a confocal microscope (SP8) with a 40x oil-water immersion objective (z step 2-3 μm, 37 °C, 6.8% CO_2).The signals were captured at the according excitation (ex) and emission (em) wavelengths: STAR-dTomato 555ex 565-601em, FRET FLII12Pglu-700uDelta6, smH3K9ac and Laconic: mTFP1/(sm)ECFP 405 ex 455-495em, mVenus/Ypet/Citrine 405 ex 514–560 em, SoNar-bound to NADH 405 ex 495–540 em, SoNar-bound to NAD^+ 488 ex 495–540 em, H1-maroon 620 ex 631–692 em, iGFP-MYC 488 ex 496–544 em (ex: excitation, em: emission).

Paraview rendering
We used Paraview for 3D renders.[106] Data tables suitable for Paraview were created per time points from the cell tracking data, containing the coordinates of the nuclei in micrometers, STAR values, as well as the cell fates. These files were then loaded into Paraview, and using the Table to Points filter they were rendered as spheres.

Validation of biosensors
To validate H2B-SoNar response, TPO3/4 STAR-dTomato-NLS H2B-SoNar organoids were cultured in glucose-free medium for 3 hours before imaging. Time-lapse imaging began with glucose-deprived organoids for at least 6 minutes before the addition of 10 mM sodium L-lactate. After 20 minutes, 10 mM sodium pyruvate was added. For smH3K9ac sensor validation, the organoids were treated with either 10 μM of A485, 2 μM of TSA, or blank-medium 7 hours prior to imaging.

RNA extraction and real-time PCR
Organoid cultures subjected to different treatments were collected in ice-cold PBS. For comparing between CSCs and CDCs, single cells were collected in PBS and were sorted based on STAR-dTomato signal (BD FACSAria™). RNA purification was performed with the RNeasy Mini Kit with DNase treatment (Qiagen), following the manufacturer's protocol. DNase treated RNA was used for cDNA synthesis using iScript cDNA synthesis kit (Biorad). Afterward, cDNA was subjected to qPCR using FastStart Universal SYBR Green Master mix (Roche) and the primers listed in Table S4.

Flow cytometry
Organoids cultures subjected to different treatments were collected in ice-cold medium and dissociated into single cells prior to flow cytometry analysis (BD FACS Celesta #660345). For mitochondrial live analysis, organoids were incubated with MitoTracker Green (500 nM) for 30 minutes at 37 °C. Stained organoids were then trypsinized into single cells and immediately analysed by flow cytometry.

Protein lysates and western blot
Organoids were collected in mix (1:1) of ice-cold PBS and Cell Recovery Solution, supplemented with 5 mM NaF and 1 mM Na_3VO_4. Upon centrifugation, pellets were lysed in lysis buffer (50 mM Tris pH 7.0, 1% TX-100, 15 μM $MgCl_2$, 5 μM EDTA, 0.1 mM NaCl, 5 mM NaF, 1 mM Na_3VO_4, 1 μg/mL Leupeptin and 1 μg/mL Aprotinin). After heat denaturation, proteins were run in SDS-PAGE and

transferred to Immobilon Polyscreen PVDF transfer membranes or Amersham Protan nitrocellulose membranes. Primary antibodies (pPDHA1 S293 1:1000, PDHA1 1:1000, H3 1:4000, H3K27ac 1:1000, H3Kpanac 1:2000, H3K9ac 1:1000, MYC/9E10 1:250, MYC/Y69 1:1000, GAPDH 1:1000, vinculin 1:10000) were applied in TBS-Tween 0.1% at 4 °C overnight followed by 1 hour RT incubation of secondary HRP-conjugated antibodies targeting either mouse or rabbit IgG in TBS-Tween 0.1% supplemented with BSA 0.5%. Protein abundance was then detected by enhanced chemiluminescence method (ECL) using ImageQuant LAS 4000mini.

Metabolomics
Sample preparation
For each sample, 1200 μL of organoid-containing matrigel or 1000 μL of cultured media were used. Organoids were washed and collected in ice-cold PBS. An equal portion of the organoid suspension was set aside for protein quantification, which was later used for normalization purposes. Organoids were centrifuged and resuspended in 80% ice-cold methanol/PBS and snap-frozen in liquid nitrogen prior to LC-MS metabolomic analysis. Medium samples were snap-frozen in liquid nitrogen immediately after collection.

Metabolomics LC-MS analysis
All organoid samples were evaporated to dryness in a Labconco Centrivap (VWR, Amsterdam, The Netherlands). To the residue 190 μL water, 10 μL 1 mM ribitol internal standard in water, 500 μL methanol and 50 μL stainless steel beads (0.9-2 mm) were added and the sample was homogenized for 2x2 min at 4 °C in a Bullet Blender (Next Advance, Troy NY, USA). After pulse centrifugation 300 μL chloroform was added and the samples were incubated for 2 hours in a VWR thermostated shaker (900 rpm, 37 °C). After centrifugation at room temperature (10 minutes, 15000xg) the upper aqueous phase was quantitatively transferred to a clean eppendorf and evaporated to dryness overnight in the Labconco Centrivap. The residue was dissolved in 100 μL water and transferred to an injection vial for LC-MS analysis. Vials were kept at 6 °C in the injector. For medium samples, 20 μL of homogenized medium was diluted with 120 μL water and sample extraction was further performed as described above.

The LC-MS analysis was performed using an Atlantis premier BEH-C18 AX column (2.1x100, 2.5 μm) connected to a related VanGuard column (Waters, Etten-Leur, The Netherlands). The column was installed into an Ultimate 3000 LC system. The column outlet was coupled to a Q-Exactive FT mass spectrometer equipped with an HESI ion source. The UPLC system was operated at a flow rate of 250 μL min−1 and the column was kept at 30 °C. The mobile phases consisted of 10 mM ammonium acetate and 0.04(v/v) ammonium hydroxide in water, pH9 (A), and acetonitrile (B), respectively. Upon 5 μL sample injection the system was kept at 0% B for 1.5 minutes followed by a 6-minute linear gradient of 0-30% B. Thereafter the gradient increased linearly to 70% in 4 minutes and kept at 70% for 0.5 minute followed by column regeneration at 0% B for 4 minutes. Mass spectrometry data were acquired over a scan range of m/z 60 to 900. The system was operated at -2.5 kV (negative mode) and 120000 mass resolution. Further source settings were: transfer tube and vaporizer temperature 350 °C and 300 °C, and sheath gas and auxiliary gas pressure at 35 and 10, respectively. For high mass accuracy mass calibration was performed before each experiment. Raw data files were processed and analysed using XCalibur Quan software.

Organic solvents were ULC-MS grade and purchased from Biosolve (Valkenswaard, The Netherlands). Chemicals and standards were analytical grade and purchased from Sigma-Aldrich (Zwijndrecht, The Netherlands). Water was obtained fresh from a Milli Q instrument (Merck Millipore, Amsterdam, The Netherlands).

Seahorse XF Flux
Seahorse Bioscience XFe24 Analyzer was used to measure oxygen consumption rates (OCR) in pmol O_2 per minute as previously described.[107] In short, organoids were seeded in 3 μL matrigel per well in XF24 cell culture microplates.

On Figures S3G and S3H, organoids were grown in control medium and treated or not with DCA (20 mM) for 24 hours prior to the experiment. Before the Seahorse run, organoids were incubated for one hour with Agient XF DMEM Medium (supplemented with 5 mM HEPES, 2 mM glutamine, 10 mM glucose, 1 mM pyruvate and B27 1:50 v/v) with or without DCA. During Seahorse run, organoids were injected with 10 μM UK5099 or medium, followed by the injections of oligomycin (5 μM), FCCP (3μM) and combination of antimycin (2 μM) and rotenone (2 μM).

On Figures S3AB, S3AC, and S3AD, organoids were grown in either control (Figures S3AB and S3AC) or lactate (Figure S3AD) conditions and treated or not with UK5099 (10 μM) for 3 days prior to the experiment. Before the Seahorse run, organoids were incubated for one hour with Agilent Seahorse XF Base Medium (supplemented with 2 mM glutamine, 17.5 mM glucose, 1 mM pyruvate and B27 1:50 v/v, pH adjusted 7.4) with or without UK5099. Consequently, organoids were injected with the combination of BPTES 20 μM and Etomoxir 40 μM (BT-ETO) or medium, followed by the injections of oligomycin (5 μM), FCCP (3μM) and combination of antimycin (2 μM) and rotenone (2 μM).

On Figures 3J and 3K, organoids were incubated one hour prior experiment with Agilent Seahorse XF Base Medium (supplemented with 2 mM glutamine, 1 mM pyruvate and B27 1:50 v/v, pH adjusted 7.4). During the Seahorse run, organoids were injected with 12 mM of D-glucose or 24 mM of L-Lactate.

On Figures 3G and S3S, organoids were cultured in lactate or control for 3 days. During the Seahorse analysis, organoids were sequentially injected with oligomycin (5 μM), FCCP (3μM) and combination of antimycin (2 μM) and rotenone (2 μM).

On Figures S3AE and S3AF, organoids were incubated for one hour prior to the experiment in glucose-deprived Agient XF DMEM Medium (supplemented with 5 mM HEPES, 2 mM glutamine, 1 mM pyruvate, and B27 at a 1:50 v/v) or in the same medium supplemented with 12 mM glucose (control). During the Seahorse assay, D-glucose was injected to bring the final glucose concentration to 12 mM in both conditions.

bulkChICseq sample preparation
TPO3-STAR-mcherry organoids were exposed to lactate medium or 20 mM of DCA for 7 hours before collecting. Treated organoids were dissociated into single cells, filtered, and resuspended in PBS buffer containing spermidine, Tween 0.05%, HEPES 20 mM, EDTA 2 mM and proteinase inhibitor (buffer C). Then cells were fixed with ethanol 100% for one hour at -20 °C, washed and stored at -80 °C in buffer C supplemented with 10% DMSO. Further steps for bulkChIC-seq sequencing were provided by Single-Cell Core of the Oncode Institute, Utrecht, the Netherlands as described previously.[108] For each condition, 100 cells were used. The data was derived from one sample for each condition.

ATACseq sample preparation and pre-processing
Organoids were cultured in either control or lactate medium for 72 hours or treated with 20 mM of DCA for 40 hours before collecting and agitating at 4 °C for 20 minutes on ice. Organoids were washed and resuspended in Recovery Cell Culture Freezing Medium (Gibco #12648-010). Then, the organoids were stored at -80 °C and sent for ATAC sequencing analysis (Vermeulan lab, Nijmegen, Netherlands). ATAC-seq was performed on approximately 100.000 cells per samples. After thawing quickly at 37 °C and washing twice with ice-cold PBS, nuclei were isolated by resuspending cells in hypotonic lysis buffer (10 mM Tris/HCL pH 7.5, 10 mM NaCl, 3 mM MgCl$_2$, 0.1% NP-40). Then ATAC-seq was performed as described in Artegiani et al.[109] Amplified DNA libraries were sequenced on an Illumina NextSeq 500.

RNAseq sample preparation
For control, lactate and DCA treated samples
The samples were prepared and collected with the same procedure as ATACseq. After pelleting, organoids were snap frozen with liquid nitrogen and sent for RNA sequencing analysis (Vermeulan lab, Nijmegen, Netherlands). RNA from snap frozen pellets was extracted using the RNeasy RNA extraction kit (Qiagen) with DnaseI treatment. A total amount of 1 μg RNA per sample was used for the preparation of RNA sequencing libraries using the KAPA RNA HyperPrep Kit with RiboErase (HMR) (KAPA Biosystems). In short, oligo hybridization and rRNA depletion, rRNA depletion cleanup, Dnase digestion, Dnase digestion cleanup, and RNA elution were performed according to protocol. Fragmentation and priming were performed at 94 °C for 6,5 minutes. First strand synthesis, second strand synthesis, and A-tailing was performed according to protocol. For the adapter ligation, a 7 μM stock was used (NextFlex DNA barcodes, Bioo Scientific). First, and second post-ligation cleanup was performed according to protocol. For the library amplification, 6 cycles were used. The library amplification cleanup was performed using a 0.8x bead-based cleanup. Library size was determined using the High Sensitivity DNA bioanalyzer (Agilent Technologies), library concentration was measured using the DeNovix dsDNA High Sensitivity Assay (DeNovix). Sequencing was performed using an Illumina NextSeq 500.
For control, lactate, control-JQ1, lactate-JQ1 samples
Organoids were cultured in either control or lactate medium for 3 days. JQ1 (100 nM) were added 6 hours before collecting. The procedure to extract RNA was done as described earlier in RNA extraction and real-time PCR. RNA samples were prepared at 15 ng/μl in MiliQ and were frozen at -80 °C and delivered to USEQ (UMC Utrecht, Netherlands) for further analysis. Sequencing was performed using an Illumina NextSeq2000.

QUANTIFICATION AND STATISTICAL ANALYSIS

Imaging analysis of fixed stains
Data analysis was performed using ImageJ. All channels were transformed into 32-bit images, smoothed and automatically thresholded.
IHC analysis
Merged images of DAPI and KRT20 channels were used to manually determine approximately equal amounts of regions of interest (ROIs) either high or low in KRT20 expression. For each image, KRT20 and MCT4 or H3K27ac or MCT1 intensity were measured per ROIs and normalized against the mean values from all ROIs.
IF analysis of stained organoids
Merged images of DAPI and KRT20 channels were used to manually create approximately equal amounts of cells of interest (COIs) either high or low in KRT20 expression. For each organoid, ratio of H3K27ac/DAPI intensity or KRT20 intensity or MCT4 intensity was calculated per COIs and normalized against the mean values from all COIs.

Single-cell analysis of organoid growth
All organoids used for single-cell analysis are in Table S2.

Single-cell tracking and intensity measurement

Time-lapse imaging (12-minute interval) of organoid development were directly sent to the OrganoidTracker tool[44] for analysis without preprocessing steps. Single nuclei were tracked using a sum of STAR and H2B-SoNar signal. Around each nucleus center at all time points, a sphere was drawn with a radius of 5 μm. The total intensity of all pixels within this sphere was measured for every fluorescent channel. Cells with low SoNar signals will be excluded from the analysis.

Cell type proportion during organoid growth

Upper and lower cutoffs (30th percentile) for cell type assignment was created using the means of the first five values in each movie. Based on these thresholds, we classified each cell at every timepoint as either High, Middle (Mid), or Low STAR and counted cell numbers for each category. For graphing purposes, we calculated the mean value for each category at every 10-timepoint interval.

STAR-SoNar correlation during organoid growth

In each organoid for every timepoint, we performed a Pearson correlation analysis between SoNar ratio and STAR signal, calculating p-values and the number of cells using the R package *stats* v.4.2.3. For visualization purposes, we organized the organoids based on the cell number captured at the first timepoint. We then presented the correlation and p-value at every 10-timepoint interval.

Classification of cell fate changes

All cells that have undergone division with their daughter cells having a minimum recorded time of 2 hours each, and all non-dividing cells with a recording time of at least 25 hours, were considered for this analysis which we called a track. Each track was classified in 4 categories: differentiation (DIFF), no-change (NC), dedifferentiation (DEDIFF) or non-defined based on 3 criteria: **slope**, **change in STAR** values and **change in cell type**. The non-defined or unknown events were excluded from the quantification. For each track, the STAR signal was normalized to the intensity at the first time point.

The **slope** was determined by fitting the smoothed STAR data (smoothing degree of 0.5) to a polynomial model, utilizing the lm() function (*stats* v.4.2.3 package).

Change in STAR was calculated by the difference between the values at the start and end of one track. Differences above 20% of STAR range of all recorded values during the movie were considered as significant change.

Changes in cell types was determined by the start and end STAR values. Stem, mid or differentiated fates of single cells are classified by the 15th percentile cutoffs of STAR values of the first 10 time points.

A track is categorized as 'DEDIFF' when the two changes are positive and the slope is greater than 0.5. Conversely, it is categorized as 'DIFF' when the changes are positive but the slope is less than -0.5. If all criteria are negative, the track is assigned as NC. In cases where at least one criterion contradicts the others, the track is manually checked. This analysis was conducted using a custom-made R script.

Symmetry division analysis

Only pairs of sister cells with a recorded duration of at least 4 hours are included in the analysis. The dynamics of STAR are considered only up to the longest observed time of the sister cell with the shorter recording period. To classify a division as asymmetric or symmetric, STAR **trend** and **difference** were used. For each sister cell, **trend** in STAR is determined by calculating the slope ("up": > 0.3 or "down": <-0.3 or "no change") and changes in STAR values (>5) between the start and end values. The **difference** in STAR between two sister cells is computed using STAR values of the final 10 time points. A division is classified as asymmetric if the STAR **trends** of two sister cells differ and the STAR **difference** exceeds 10. Otherwise, the division is classified as symmetric.

Cell cycle length

Cell cycle duration was determined by tracking the time between consecutive divisions for all cells throughout the entire video, where both the initial and subsequent divisions were observable.

Dividing rate overtime

For every 1 hour throughout the videos, percentage of dividing events relative to total cell count (determined from the initial time point of the period) was calculated. These measurements were then clustered based on organoid size ranges, as indicated on the x-axis.

Clone size analysis

All cell lineages that span at least 50 hours are included in this analysis. All events happening after 50 hours were excluded. Number of divisions were counted in each lineage tree. The clone size of the cell that started the lineage tree is then defined as the number of divisions in the lineage tree plus 1.

Single-cell analysis of metabolic dynamics

Nuclear lactate (Laconic-NLS) and NAD⁺/NADH (H2B-SoNar)

Single cell 3D measurements for each channel: mTFP1, mVenus, SoNar-bound to NADH, SoNar-bound to NAD$^+$ and STAR were obtained using OrganoidTracker tool.[44] Cells with low signals of two FRET channels were excluded. Cells were categorized into STAR^{pos} - CSC and STAR^{neg} - CDC groups using a 30th percentile cutoff, based on the average STAR values from the initial three measurements.

To assess lactate changes following lactate injection (10 or 20 mM of sodium L-lactate) with or without MCT1 inhibition (AZD3965 1 μM), organoids were pre-incubated in glucose-free medium for 3 hours prior to imaging (2.5-minute interval). Uptake capacity of lactate or SoNar changes (2-minute interval) between the two cell types were determined by differences of FRET or SoNar signals between post-treatment and pre-treatment normalized to the pre-treatment values. In Figure S1Y, Pearson correlation between basal lactate levels and lactate uptake capacity was calculated after removing outliers using the Z-score method with a threshold of 3.

To assess lactate response to dual inhibition of MCT1 and MCT4 (Figure 1H), organoids were first cultured under control conditions, and baseline images were captured. Post-treatment images were acquired following a 3-hour treatment with 10 μM Syrosingopine. Average single-cell measurements were calculated between the two cell types for each organoid.

Cytosolic glucose (FLII12Pglu-700uDelta6)

To measure the cytosolic glucose signal (FRET ratio, Citrine/ECFP), the cytoplasm was segmented using sum of ECFP and Citrine channels (Gaussian filter radius = 1.5 px, Sauvola local threshold k = 0.05).[110] To perform single-cell measurements, we first manually tracked the center points of all nuclei over time. Then, for every cell at every time point we measured the ECFP and Citrine cytosolic signals and the STAR nuclear signal within 5 μm from the center points. A pixel could only be assigned to a single cell; if a cytoplasm pixel was within 5 μm of two cell centers, the nearest cell center was chosen. To assess glucose changes following glucose injection (10 mM and 20 mM of D-glucose), organoids were pre-incubated in glucose-free medium for 6 hours prior to imaging (4-minute interval). Subsequent analysis was carried out comparably to the approach used for measuring nuclear lactate and NAD$^+$/NADH.

Single-cell analysis of H3K9ac

Static images of TPO3/4 STAR- dTomato-NLS smH3K9ac H1-maroon were captured (z-step 2 μm). Single cell FRET measurements were calculated by Ypet/smECFP ratio in the nuclear fractions. The nuclei were segmented using the merged image of H1-maroon and STAR-dTomato using StarDist 2D.[104] Three-dimensional reconstruction of the nuclei was executed using a distance-based method through a custom R script. Cells with low FRET signal were excluded. Cells were categorized into STARpos and STARpos groups using a 30th percentile cutoff. Mean values for each organoid were calculated from data of all single cells. To assess nuclear H3K9ac changes following lactate injection, TPO3 organoids were pre-incubated in glucose-free medium for 3 hours and the images of the organoids were captured at 0, 8 and 16 hours after the lactate injection. For the sensor validation, the intensity was calculated for each organoid as the mean value of all the 3D-generated nuclei.

scRNAseq analysis

Cell type assignment and metabolic score calculation

Sixty-five scRNA datasets (see Table S5) were obtained from the following sources: GEO: GSE178341,[24] GEO: GSE196964,[22] GEO: GSE161277.[23] Datasets with low number of epithelial cells (< 200) were excluded from the analysis. Data of each tumour was processed individually using Seurat v4.3.[111] First, filtering was applied such that all remaining cells had between 200 and 5000 features, and less than 15% of mitochondrial genes. Subsequently, the data was normalized and scaled using the standard procedures provided in the Seurat package. The analysis was continued using only the epithelial cells: we manually selected all cells in the clusters that were clearly positive for *KRT8* and *EPCAM*. For cell type assignment, we applied the algorithm of scType.[112] Cell types were determined based on both the colon cancer based-gene sets established by Zowada et al.[52] and the built-in gene sets of scType[112] (see Table S6). Cells were specifically classified as Stem, Paneth, TA, or Terminally-differentiated (T-diff) based on the highest Zowada et al. scores. For further clarification, Paneth cells were relabeled as Secretory. T-diff cells were subsequently reclassified as either Enterocytes or Secretory, contingent on whether the scType clustering indicated Goblet cells. Then, the "module score" were computed for each single cells for various metabolic gene sets (as referenced in the figure legend) using the AddModuleScore function from Seurat (control features n = 100). Moreover, using the scaled data, we recorded the scaled expression of the following genes: *ASCL2, LGR5, KRT20, SLC16A3 (MCT4)* and *KI67*. Expression is calculated by the average values of all epithelial cells within the tumour. Outliers were removed using the ROUT method prior to visualization and statistical analysis.

Microarray sample signature scoring

The datasets of 290 and 96 patients with CRC were used from the following sources: GEO: GSE14333[65] and GEO: GSE33113[66] for this analysis. Data was normalized using RMA normalization and extracted using affy v1.76.0[113] and Biobase v1.58.0 packages.[114] Then we annotated Affymetrix probesets to gene symbols using biomaRt v2.54.1 package.[115] All duplicated genes were replaced by the highest expressing ones. Then signature scores were calculated using Single-sample Gene Set Enrichment Analysis (ssGSEA) from GSVA v1.46.0 package.[69] Pearson correlations between two MYC gene sets V1/V2 and several metabolic or signaling gene sets were calculated. More information of the signature gene sets can be found in Table S6.

Real-time PCR analysis

The relative expression of individual genes, compared to expression levels under control conditions, was determined using the 2$^{-\Delta\Delta Ct}$ method from Ct readouts for each gene, normalized to housekeeping genes (as mentioned in the legend).

Metabolomics analysis

Metabolite levels in organoids were normalized by protein amount (determined by Bradford protein assay #Biorad, otherwise stated in the legend) and normalized to the control conditions. Metabolite levels in the media were subtracted to the starting level of the metabolites in starting medium and then normalized to the control conditions. Data is represented as log$_2$ fold change in Figures 3B and S3F or in fold change in Figures S1K, S2C, S2L, S3A, S3C, and S4AD.

Seahorse analysis

For analysis, all the wells showing negative values after background correction were excluded. OCR and EACR values were normalized to the average DNA amount of each condition. Basal respiration was calculated by the differences between the last two measurements after rotenone/antimycin A injection and the first measurement before oligomycin treatment. Maximal respiration was calculated by the differences between the measurements before and after rotenone/antimycin A treatment. Spare respiratory capacity% were calculated by (Maximal respiration/basal respiration) x 100.

bulkCHICseq data preprocessing and analysis

Adapters were removed for all libraries and bulkChIC reads are mapped with bwa-mem[116] (v0.7.16a) to HG38 and sequences of common contaminants: Cutibacterium, E. coli K-12, Escherichia virus Lambda, and E. coli RHB09-C15. Next, the reads are deduplicated and fragments are filtered using SingleCellMultiOmics[117] bamtagmultiome.py (v0.1.26). Reads mapping to problematic genomic regions or contaminants are removed. Problematic genomic regions are identified using the ENCODE blacklist.[118] The counts were extracted as reads mapping into transcription start sites (TSS) with 2kb upstream of a gene body. Regions with lower than 30 counts were excluded and $\log_2$ fold change (log2FC) were calculated between lactate and control-cultured organoids. Then we rank all the genes in the order of log2FC. We applied the same strategy for DCA treated condition (with the exception of *MYC* having an FDR = 0.06).

ATACseq analysis
Differential expression

Raw sequencing reads were processed and aligned to the human genome (HG38) with the seq2science[119] (v0.7.2) ATAC-seq pipeline with default settings. Bam files of aligned reads were used to extract counts for each gene (the whole genebody ± 5kb) using featureCounts function from Rsubread package (v2.12.3).[120] Raw counts were used as input for DESeq2[121] (v1.38.3) to perform normalization and differential gene expression analysis for each treatment (lactate or DCA 20 mM) compared to control organoids. Genes with lower than 75 counts were excluded from the analysis. Relative expression of significant transcripts (p-value < 0.01) was illustrated with ComplexHeatmap.[122]

ATACseq signal in upregulated and random transcripts

ATAC $\log_2$FC values of all genes were derived for each treatment (lactate or DCA 20 mM) relative to control organoids. These values were grouped into either Upregulated transcripts identified in the RNA-seq analysis or Random transcripts generated using the random_query() function from the gprofiler2[123] package v0.2.1. Genes with fewer than 100 counts of ATAC-seq were excluded from the analysis. Due to space limitations, not all histones are shown. To evaluate the statistical significance of the distribution differences between the two groups, Wilcoxon test was used. The statistical test was performed on 20 pairs of Random and Upregulated groups (n = 95), each Random group contains approximately 100 genes.

RNAseq analysis
For control, lactate and DCA treated samples

Raw sequencing reads were aligned to the human genome (HG38) with hisat2.[124] PCR duplicates were removed with Picard[125] and transcripts were quantified with htseq.[126] Raw counts were used as input for DESeq2[121] to perform differential gene expression analysis of each treatment compared to control organoids. Relative expression of significant transcripts (adjusted p-value < 0.05) was illustrated with ComplexHeatmap.[122]

For control, lactate, control-JQ1, lactate-JQ1 samples

Quality control on the sequence reads from the raw FASTQ files was done with FastQC[127] (v0.11.8). TrimGalore[128] (v0.6.5) as used to trim reads based on quality and adapter presence after which FastQC was again used to check the resulting quality. rRNA reads were filtered out using SortMeRNA[129] (v4.3.3) after which the resulting reads were aligned to the reference genome fasta (GCA_000001405.15_GRCh38_no_alt_analysis_set.fna) using the STAR[130] (v2.7.3a) aligner. Follow up QC on the mapped (bam) files was done using Sambamba[131] (v0.7.0), RSeQC[132] (v3.0.1) and PreSeq[133] (v2.0.3). Read counts were then generated using the Subread FeatureCounts module[134] (v2.0.0) with the Homo_sapiens.GRCh38.106.ncbi.gtf gtf file as annotation. Raw counts were used as input for DESeq2[121] to perform normalization and log transformation. Differential gene expression analysis of all treatment was compared using one-way ANOVA (stats v4.2.3 package). Relative expression of significant transcripts (adjusted p-value < 0.05) was illustrated with ComplexHeatmap.[122]

Gene ontology analysis of sequencing data

Gene ontology analysis was done by uploading the significantly upregulated or downregulated gene lists to ShinyGO v0.61 and ShinyGO v0.77. Hit percentages were calculated as the number of detected genes over the total genes in the pathway x100. Only interested pathways are depicted in the plots (see Table S7 for additional significant pathways).

Statistical Analysis

Statistical analysis for image analysis, flow cytometry, seahorse and metabolomics results was performed by using Graphpad Prism 9 and 10. First Gaussian distribution of data was tested to next apply parametric or non-parametric statistics. Statistical analysis for sequencing (ATACseq, RNAseq, microarray) analysis was performed by different packages in R as stated. Details of statistics and sample sizes are described in the figure legends.